Iranian Neo-Tethyan magmas as a significant CO_2 source during the Middle Eocene Climate Optimum

Lea Ostorero[1*], Rosario Esposito[1], Pierre Bouilhol[2], Paolo Ballato[3], Veleda Astarte Müller[4], Maria Luce Frezzotti[1], Pietro Sternai[1,5]

[1]Department of Earth and Environmental Sciences - DISAT, University of Milano-Bicocca, Piazza dell'Ateneo Nuovo, 1 – 20126, Milan, Italy
[2]Université de Lorraine, CNRS, CRPG, F-54000 Nancy, France
[3]Department of Science, Roma Tre University, Roma, Italy
[4]Department of Geosciences, University of Arizona, Tucson, USA
[5]GFZ German Research Centre for Geosciences, Potsdam, Germany

[*]Corresponding author: leaemma.ostorero@unimib.it

Highlights

- First measurements of volatile content in Eocene Neo-Tethyan lavas from Iran.
- 1.01×10^{19} g CO_2 (minimum estimate) were released from the studied magmas.
- The degassed CO_2 likely contributed to the Middle Eocene Climatic Optimum.

Abstract

CO_2 emissions from magmatic arcs can affect the atmosphere composition, thereby driving long-term global climate changes. Early Cenozoic climate trends are generally associated with changes in global silicate weathering related to Neo-Tethyan geodynamics, but the likely climatic effects of changes in degassing from Neo-Tethyan magmatic arcs have been poorly quantified. Here, we characterize the petrography and provide the first measures of the volatile content (CO_2, H_2O, F, Cl and S) of pre-eruptive melts based on glassy, bubble-bearing and reheated melt inclusions within plagioclase and clinopyroxene crystals in Early Cenozoic trachyandesites from the Alborz and Tabriz regions (Iran). CO_2 concentrations in these melt inclusions reach up to 6733 ppm, thus providing a minimum estimate of the total amount of CO_2 degassed from Iranian magmas during the middle-late Eocene of 1.01×10^{19} g CO_2, with a total C flux released of 0.306 (± 0.012) Mt C/yr, which is within the carbon imbalance predictions estimated based on other proxies. Our measures validate earlier hypotheses that magmatic CO_2 degassing from the targeted igneous provinces contributed to the Middle Eocene Climatic Optimum. Further measurements of the volatiles content of Neo-Tethyan magmas are thus critical to assess the drivers of Early Cenozoic climate trends and understand the global volatile cycling over geological timescales.

Keywords: melt inclusion, volatiles, heating experiment, trachyandesite, CO_2 degassing, Middle Eocene Climate Optimum

Iranian Neo-Tethyan magmas as a significant CO_2 source during the Middle Eocene Climate Optimum

Lea Ostorero[1*], Rosario Esposito[1], Pierre Bouilhol[2], Paolo Ballato[3], Veleda Astarte Müller[4], Maria Luce Frezzotti[1], Pietro Sternai[1,5]

[1]Department of Earth and Environmental Sciences - DISAT, University of Milano-Bicocca, Piazza dell'Ateneo Nuovo, 1 – 20126, Milan, Italy
[2]Université de Lorraine, CNRS, CRPG, F-54000 Nancy, France
[3]Department of Science, Roma Tre University, Roma, Italy
[4]Department of Geosciences, University of Arizona, Tucson, USA
[5]GFZ German Research Centre for Geosciences, Potsdam, Germany

[*]Corresponding author: leaemma.ostorero@unimib.it

Highlights

- First measurements of volatile content in Eocene Neo-Tethyan lavas from Iran.
- 1.01×10^{19} g CO_2 (minimum estimate) were released from the studied magmas.
- The degassed CO_2 likely contributed to the Middle Eocene Climatic Optimum.

Abstract

CO_2 emissions from magmatic arcs can affect the atmosphere composition, thereby driving long-term global climate changes. Early Cenozoic climate trends are generally associated with changes in global silicate weathering related to Neo-Tethyan geodynamics, but the likely climatic effects of changes in degassing from Neo-Tethyan magmatic arcs have been poorly quantified. Here, we characterize the petrography and provide the first measures of the volatile content (CO_2, H_2O, F, Cl and S) of pre-eruptive melts based on glassy, bubble-bearing and reheated melt inclusions within plagioclase and clinopyroxene crystals in Early Cenozoic trachyandesites from the Alborz and Tabriz regions (Iran). CO_2 concentrations in these melt inclusions reach up to 6733 ppm, thus providing a minimum estimate of the total amount of CO_2 degassed from Iranian magmas during the middle-late Eocene of 1.01×10^{19} g CO_2, with a total C flux released of 0.306 (± 0.012) Mt C/yr, which is within the carbon imbalance predictions estimated based on other proxies. Our measures validate earlier hypotheses that magmatic CO_2 degassing from the targeted igneous provinces contributed to the Middle Eocene Climatic Optimum. Further measurements of the volatiles content of Neo-Tethyan magmas are thus critical to assess the drivers of Early Cenozoic climate trends and understand the global volatile cycling over geological timescales.

Keywords: melt inclusion, volatiles, heating experiment, trachyandesite, CO_2 degassing, Middle Eocene Climate Optimum

1. Introduction

On timescales of millions to tens of millions of years, the geological carbon cycle controls how much carbon is stored into rocks and how much carbon is released into the ocean and atmosphere (Berner and Lasaga, 1989; Sundquist, 2013). Plate tectonics and magmatism are

thus linked to the evolution of climate and life, as volcanoes and magmatic provinces are sources of carbon by releasing greenhouse gases [e.g., carbon dioxide (CO_2)], as well as H_2O, sulfur, and halogens [e. g., F, Cl, Br] (Berner, 2003; Berner and Lasaga, 1989; Burton et al., 2023; Cloetingh et al., 2023; Walker et al., 1981). CO_2 is one of the major components of volcanic gases and evidence for higher carbon output was shown for arcs where carbonate sediments subduct (Freundt et al., 2014) or where magma-carbonatic rocks interactions occur in the upper crust (Aiuppa et al., 2017). Understanding the long-term interactions between climate and magmatism is also critical to locate and manage natural resources as well as mitigate natural hazards, but the relationships between continental subduction/collision and magmatic activity are, to date, particularly poorly constrained (Sternai, 2023).

During the Paleocene and early Eocene, approximately from 60 Ma to 50 Ma, a climate warming trend is observed, followed by a 15 Myr period of cooling, between 50 and 35 Ma (Beerling and Royer, 2011; Hansen et al., 2013; Zachos et al., 2001). The Eocene cooling trend is classically ascribed to atmospheric CO_2 consumption by tectonic uplift, erosion and silicate weathering that occurred along the Eurasian Margin in relation with the India-Eurasia collision (Raymo and Ruddiman, 1992). Eocene cooling, however, is perturbed by a significant sharp temperature increase anomaly at ~40.5 Ma lasting 500 kyr and referred to the Middle Eocene Climatic Optimum (MECO) (Ma et al., 2024; Simon et al., 2008; Sluijs et al., 2013; van der Boon et al., 2021). Although more than 15,000 km of magmatic arcs were active along the convergent Neo-Tethyan plate margins throughout the Mesozoic and the Paleogene (Seton et al., 2012; Sternai et al., 2019), the possibility that the considerable and variable amount of CO_2 sourced from these arcs into the ocean and atmosphere contributed to global climate was only marginally explored thus far (Hoareau et al., 2015; van der Boon et al., 2021; Zhang et al., 2023). Interestingly, magmatic flare-ups from the Neo-Tethyan arcs in Iran occurred between ~50-35 Ma, peaking around 45-40 Ma (Alpaslan et al., 2004; Arslan and Aslan, 2006; Kazmin et al., 1986; van der Boon et al., 2021; Verdel et al., 2011; Vincent et al., 2005), which overlaps with the MECO. Previous authors suggested that intensified volcanic activity in Iran may have contributed to the MECO (Bohaty et al., 2009; van der Boon et al., 2021). However, this hypothesis remains largely untested by direct measurements, which are only possible through melt inclusions (MI) to assess the pre-eruptive volatile content of melts (Esposito, 2021, and references therein). Melt inclusions are melt droplets trapped in crystals during their growth (Esposito, 2021; Metrich and Wallace, 2008, and references therein). The preserved pre-eruptive volatile content of magmas can be used to assess the storage conditions of magmas and estimate the CO_2 outgassing for magmatic systems where MI can be retrieved (Balcone-Boissard et al., 2023; Esposito, 2021; Esposito et al., 2023, 2011; Hauri, 2002; Lowenstern, 1995; Metrich and Wallace, 2008; Putirka, 2008; Roedder, 1979; Rose-Koga et al., 2021; Sobolev, 1996; Sobolev and Danyushevsky, 1994).

Here, we present the first measurements of CO_2 concentrations within MI in plagioclase and clinopyroxene crystals from Eocene Iranian trachyandesites. These measures enable us to constrain the pre-eruptive volatile content of Eocene Iranian lavas and provide the first volatile-based estimate of the regional magmatic CO_2 emissions to evaluate the proposed Iranian magmatic forcing on the MECO (De Leeuw, et al., 2007; Hilton, et al., 2002; Sano & Williams, 1996; Wallace, 2005).

2. Regional geology of Iran

Iran is located on the Arabia-Eurasia plate margin, an extensive region that is actively deforming due to ongoing continental collision following the subduction of the Neo-Tethys Ocean (Agard et al., 2005; Hatzfeld and Molnar, 2010; Vernant et al., 2004). The northward subduction of oceanic lithosphere beneath Iran occurred at fairly constant rates, between 2 and 3 cm/yr, since ~56 Ma (McQuarrie et al., 2003). The timing of collision onset between Arabia and Eurasia remains controversial; early works proposing from the Late Cretaceous to the Miocene or even the uppermost Pliocene (Alavi, 1994; Berberian et al., 1982; Berberian, 1983; Berberian and King, 1981; Falcon, 1974; Stöcklin and J., 1968), whereas more recent studies seem to agree on a late Eocene-Oligocene collision initiation (Agard et al., 2011, 2005; Ballato et al., 2011; Fakhari et al., 2008; Jolivet and Faccenna, 2000; Koshnaw et al., 2019; McQuarrie and van Hinsbergen, 2013; Pirouz et al., 2017; Verdel et al., 2011; Vincent et al., 2005). Regardless of its onset timing, the Arabia-Eurasia collision mainly led to the formation of the Zagros, Caucasus, Alborz, Kopeh-Dag and Talesh mountains in Iran (Boutoux et al., 2021; Hatzfeld and Molnar, 2010) (**Fig. 1**).

During the Paleogene, subduction of the Neo-Tethyan oceanic lithosphere beneath Iran at rates of 2-3 cm/yr produced the 'Andean-type' Urumieh-Dokhtar arc in Central Iran, extending over ~1500 km (Boutoux et al., 2021; Dewey et al., 1973; McQuarrie et al., 2003). The Urumieh-Dokhtar belt is one of the three areas in Iran where Eocene calc-alkaline volcanic rocks are preserved, along with the southern Alborz Mountains, and the Lut block of eastern Iran, with an overall estimated volumes of magmatic material in the order of 10^6 km^3 (Verdel et al., 2011) (**Fig. 1**). The Alborz mountains extend from Talesh in the west, where they are characterized by a back-arc system signature (Asiabanha and Foden, 2012; Golonka, 2004; Vincent et al., 2005), to Kopet Dagh in the east (van der Boon et al., 2017). Evidence of submarine volcanism has been reported in the Alborz mountains where at least 3000- to 4000-m-thick volcanic, volcaniclastic and sedimentary strata currently outcrop, as the Karaj Formation where locally up to 8000 m of volcanoclastic sediments are present (Amidi et al., 1984; Amidi and Michel, 1985; Ballato et al., 2013; Berberian and King, 1981; Förster et al., 1972; Verdel et al., 2011). Previous works in this region also show mafic to intermediate andesitic and dacitic lavas associated to a magmatic pulse in the Eocene (Amidi et al., 1984; Amidi and Michel, 1985; Azizi and Jahangiri, 2008; Förster et al., 1972; Verdel et al., 2011), preceded and followed by minor or no magmatism (Pearce et al., 1990). While previous studies have estimated the pressure and temperature storage conditions of Oligocene magmas from Urumieh-Dokhtar magmatic arc and Quaternary volcanic rocks (Babazadeh et al., 2021; Salehi et al., 2020), the Eocene volcanics are less studied and their volatile content is currently unconstrained. Our study focuses on Eocene volcanic rocks located along the northwestern sector of the Iranian Plateau (north of the city of Tabriz) and the southern flank of the Alborz mountains (Karaj Formation) (**Fig. 1**).

A widespread magmatic flare-up that delivered a large fraction of the total magmatic production occurred throughout Iran in the Eocene, despite a relatively slow and steady rate of subduction (Azizi and Moinevaziri, 2009; Ducea, 2001; Ducea and Barton, 2007; Verdel et al., 2011). The cause of this flare-up has been long debated (Amidi et al., 1984; Amidi and Michel, 1985; Förster et al., 1972; Shafaii Moghadam et al., 2015). By combining new age constraints and geochemical data from primitive mafic rocks emitted during and after the flare-up, Verdel

et al. (2011) proposed a model where Eocene extension and crustal thinning, accompanying slab rollback generated decompression melting of a lithospheric mantle hydrated by slab-derived fluids (see also Shafaii Moghadam et al., 2015). A similar dataset led Rabiee et al. (2020) to propose that upwelling in the back-arc region generated asthenospheric melt, which interacted with the metasomatized supra-subduction mantle wedge and/or the continental crust, resulting in magma with heterogeneous characteristics.

Van der Boon et al. (2021) explored the link between the Iranian magmatic arc flare-up and the MECO, and estimated the total amount of carbon released during the flare-up between 1052-12565 Pg C using the spatial extent of presently outcropping volcanic rocks as a base to constrain the total volume of erupted volcanics. It should be noted, however, that this estimate most likely represents minimum values because endorheic conditions persist in Central Iran, where volcanic rocks are probably buried beneath a several-kilometer-thick sequence of late Cenozoic marine and continental sediments. Nevertheless, this estimate matches the amount of carbon released required to produce the MECO (Henehan et al., 2020; Sluijs et al., 2013; van der Boon et al., 2021; van der Ploeg et al., 2018). However, the CO_2 content of the magmas associated with the Eocene magmatic flare-up in Iran was not directly quantified (van der Boon et al., 2021). Hence, direct petrological measurements are required to verify the possible links between the Eocene Iranian flare-up and the MECO.

3. Material and methods

The analyzed samples include three trachyandesitic samples from the NW sectors of the Iranian Plateau, in the region of Tabriz and the southern Alborz Mountains, representing the back-arc of the Eocene subduction system (**Fig. 1; Supplementary Fig. 1;** their coordinates are provided in **Table 1**) (Geological Survey and Mineral Exploration of Iran, 2006, 1995). Geological maps constrain the samples ages to the middle-late Eocene (Geological Survey and Mineral Exploration of Iran, 2006, 1995). The samples have been cut for thin sections (University of Milano-Bicocca and Petrolab, Sardegna), crushed for grains separation, and grinded for powder (whole rock analyses). Minerals were separated using a Frantz magnetic separator and handpicked under a stereomicroscope. The next steps of MI preparation as well as Raman, SIMS, and microprobe analyses are presented below and in more details in the **Supplementary Note 1**.

3.1. Whole rocks

Whole rock major-element compositions were analyzed using an inductively coupled plasma optical emission spectrometer (ICP-OES) at Bureau Veritas Mineral Laboratories (Canada). Oxides that were characterized are SiO_2, TiO_2, Al_2O_3, Fe_2O_3, MnO, CaO, Na_2O, K_2O and P_2O_5. Internal standards from Bureau Veritas were used for calibration.

3.2. Melt inclusions preparation

MI bearing samples were prepared in the laboratory of the University of Milano-Bicocca, and sample preparation details are reported in the **Supplementary Note 1**.

Crystals of plagioclase and clinopyroxene were mounted individually in Crystalbond 509 on a heating plate. If the MI in the crystals were homogeneous, each crystal was polished again to expose the targeted MI (**Supplementary Fig. 2**). If the MI were crystallized, heating experiments were performed, and after the experiment, quenched MI were exposed to the surface of the crystals by gently polishing them (**Supplementary Fig. 2-3;** see below). A second extraction of the crystals from the Crystalbond was carried out to press the crystals with the exposed MI in an indium mount for analysis of volatiles in the MI glasses to prevent epoxy contamination driven by low-vacuum by Secondary Ion Mass Spectrometry (SIMS).

3.3. Heating experiments

Melt inclusions in the Iran trachyandesites (**Table 1**) required heating and quenching to obtain a homogeneous glass, as MI are partially or totally crystallized in all plagioclase crystals and some of the clinopyroxene crystals. Heating of the MI was necessary as analyzing crystallized MI can generate misleading information about the original melt composition and volatile content (Esposito et al., 2023). 33 heating experiments were conducted at University of Milano-Bicocca (Italy) using a one-atmosphere Linkam TS1400XY heating stage (Esposito et al., 2012). The heating stage was mounted on a petrographic microscope, as described in other studies (Esposito et al., 2016; Klébesz et al., 2015). The heating procedure consisted in an increase of the temperature of a crystal (with one or more MI) from room temperature up to the temperature for melting crystals inside the MI to reverse the crystallization that occurred after MI entrapment (Narváez et al., 2023) (**Table 2; Supplementary Fig. 3; Supplementary Note 1**). The experiments lasted from 2 to 3 hours, with relatively fast heating rates and a limited duration for each heating plateau (**Table 2**). The cooling rate after quenching the experiment is of ~190 °C/min. After the experiments, MI of interest were exposed on the surface of crystals.

3.4. Raman analyses

Vapor bubbles in 30 bubble-bearing MI studied here were analyzed for volatile contents using Raman spectroscopy with a Horiba Jobin Yvon LabRAM HR Evolution Raman System at the Department of Earth and Environmental Sciences, University of Milano-Bicocca (Italy) (see **Supplementary Note 1** for more details). CO_2 spectra were recorded using a green Nd 532.06 nm laser source, powered at 150 mW by mean of the 25% neutral density filter, with a 100 × magnification. Spectra have been acquired by one accumulation of 30 or 60 seconds each. Spectra have been treated with baseline correction with a pseudo Voight function (Yuan and Mayanovic, 2017) by the freeware software Fityk 1.3.1 (https://fityk.nieto.pl/) (Wojdyr, 2010). The presence of CO_2 in bubbles in bubble-bearing MI is characterized by two bands at ~1285 cm^{-1} and ~1388 cm^{-1}, the Fermi doublet and two symmetrical weak bands below 1285 and above 1388 cm^{-1} (Colthup et al., 1975). The distance between the Fermi doublet is proportional to fluid density (Frezzotti et al., 2012; Garrabos et al., 1980). Several calibrations have been proposed for calculating the density of CO_2 fluid inclusions and in this study, we used the densimeter of Remigi et al. (2021). The CO_2 content of the vapor bubbles can then be calculated using the mass ratio between bubble and glass in the hosted MI (Esposito et al., 2011; Hartley et al., 2014; Moore et al., 2015), with the following equation:

$$[CO_2]_{bubble} = \frac{M_{bubble}^{CO_2}}{M_{glass}} * 10^6 = \frac{V_{bubble} * CO_{2,density}}{V_{glass} * Melt_{density}} * 10^6 \#(1)$$

Where we use an estimated $Melt_{density}$ of 2.32 g.cm^{-3}, using the Igpet software (Carr and Gazel, 2017), V_{bubble}, which is the bubble volume, V_{glass}, the volume of the glass and $CO_{2,density}$ is the measured fluid density (**Supplementary Table 1**).

3.5. Analyses of volatiles by SIMS

Volatile (CO_2, H_2O, F, S, Cl) and Al concentrations of the glass in reheated MI were determined on an indium mount with the exposed MI of all crystals, using Secondary Ions Mass Spectrometry (SIMS), Cameca 1280 at Centre de Recherches Pétrographiques et Géochimiques (Nancy, France) (see **Supplementary Note 1** for more details). These analyses were performed before EPM, to prevent a potential carbon contamination from carbon coating. Indium mounts were dried in a vacuum-oven for 12h at 40 °C and each sample was gold-coated. Cs^+ was used as the primary ion source with the use of electron gun and a primary beam intensity of 0.5 nA. The contrast and field apertures were of 400 µm and 1200 µm, respectively and the mass resolving power was of 7007. The counting times on each mass of elements were of 4 s for ^{12}C, ^{16}O, ^{1}H, ^{32}S and ^{35}Cl, 2.96 s for ^{18}O, ^{27}Al and ^{30}Si and 4.96 s for ^{19}F. Each analytical spot was pre-sputtered for 300 s to clean the surface before analysis and the deadtime applied was of 35 ns. Detection limits are of 0.01 wt% for H_2O, 42 ppm for CO_2, 10 ppm for F, 2 ppm for S and 31 ppm for Cl. The analytical accuracy was calculated based on the average deviation of the individual reference glasses from calibration curves. This deviation was 1 % for CO_2, 2 % for H_2O, 2 % for F, 2 % S and 3 % for Cl. The high CO_2 contents measured in the MI of our study (> 3000 ppm) had a $^{12}C^+$ signal that was stable during SIMS analysis, which is consistent with high intrinsic CO_2 contents rather than a contamination from surficial carbon.

3.6. Electron microprobe analysis of MI and host crystals

The compositions of the crystals and glasses were obtained using an electron microprobe (EMP; Jeol 8200 at the Earth Sciences Department, University of Milan), after SIMS analyses (see **Supplementary Note 1** for more details). For residual glasses and MI, alkalis were analyzed first to minimize their migration under the electron beam. The EMP analytical conditions were set to an acceleration voltage of 15 kV, a beam current of 5 nA, a focused beam (spot size of ~1 µm) for minerals and a defocused 5-µm diameter beam size for glasses. For all elements, peak and background counting times, were set to 30 and 10 s, respectively. The oxides analyzed were Na_2O, K_2O, SiO_2, Al_2O_3, TiO_2, FeO, MgO, CaO, MnO, NiO, P_2O_5 and Cr_2O_3. The host mineral compositions were analyzed close to the MI. Typical analytical errors on major elements are 1% for CaO and K_2O, 2% relative for SiO_2, MgO and Al_2O_3, 3% for Na_2O, MnO, TiO_2, FeO, Cr_2O_3 and NiO and 4% for P_2O_5.

3.7. Temperature/pressure estimations

The equilibrium temperatures were estimated using the equations 33 for clinopyroxene-liquid thermometer and the equation 24a for plagioclase-liquid thermometer from Putirka (2008). The standard deviations of the estimates reported by Putirka (2008) are ± 41°C and 36°C, respectively. The fluid-saturation pressure of each MI was estimated using H_2O and CO_2

volatile contents and MagmaSat (Ghiorso and Gualda, 2015). These temperature and pressure values were compared to the ones found based on the clinopyroxene-liquid thermometers and barometers for alkaline differentiated magmas from Masotta et al. (2013).

4. Results

4.1. Samples and petrography of the MI

The analyzed trachyandesites present a 55.8-56.5 wt% SiO_2 content and a 7.4-9.1 wt% Na_2O+K_2O content (**Fig. 2; Table 3**). Samples from Tabriz have between 10 and 24 vol% of phenocrysts. These crystals are mainly plagioclase crystals up to 1 mm in size (6-7 vol%), pyroxene up to 500 µm (0.5-2 vol%), few oxides (0.1-1 vol%) and altered minerals such as altered amphibole and co-existing biotite (2-14 vol %). The Alborz sample has ~62 vol% of crystals with millimetric to centimetric plagioclase (58 vol%), altered amphiboles and co-existing biotite (3 vol%), clinopyroxene up to 700 µm (< 1 vol%), as well as few oxides (0.5 vol%) (**Supplementary Note 1**).

Melt inclusions are partially or highly crystallized in plagioclase crystals from the trachyandesites, being completely opaque while they are homogeneous or containing small crystals in clinopyroxene crystals (**Supplementary Fig. 3**). Petrographic descriptions of the MI found in plagioclase and clinopyroxene, and other information on individual MIs and their host crystals are listed in **Supplementary Table 1** and in the **Supplementary Note 2**. MI are mostly ellipsoidal in shape. Sizes and volumes of the MI have been estimated, as well as bubble sizes and volumes for bubble-bearing MI (**Supplementary Fig. 4**). Most of the MI in clinopyroxene and plagioclase crystals are between 3 and 22 µm in length.

For Alborz, 30 % of the MI that are hosted in heated plagioclase are between 3 and 22 µm, while the rest of the MI in plagioclase are between 22 and 140 µm (**Supplementary Fig. 4**). These MI reach the highest length, as 10% of MI in plagioclase from Alborz vary between 98 and 140 µm (**Supplementary Fig. 4**). The same relationship is observed for MI in clinopyroxene for Alborz, where 50 % of them are between 3 and 22 µm in length and the rest of the MI are up to 98 µm in length (with a lower percentage). For Alborz, 86 % of the MI in heated plagioclase are bubble-bearing, while 14 % are glassy. For clinopyroxene from Alborz, only 30 % of the MI are bubble-bearing (**Supplementary Table 1**). The distribution of the bubble volume fractions for Alborz mostly have a peak at 1 vol% (35 and 37 % for clinopyroxene and plagioclase, respectively), which is lower than the threshold corresponding to shrinkage bubbles formed by post-entrapment modifications (< 5 vol. %) (Lowenstern, 2003, 1995) (**Supplementary Fig. 4; Supplementary Note 2**).

For Tabriz, 60 % of the MI in heated plagioclase are measuring 3 to 22 µm, while 30 % are between 22 and 41 µm and the rest is up to 79 µm (**Supplementary Fig. 4**). For clinopyroxene, 50 % of the MI are 3 to 22 µm in length while the rest are measuring up to 60 µm (**Supplementary Fig. 4**). For Tabriz, 70 % of the MI in heated plagioclase are bubble-bearing while all clinopyroxene-hosted MI are glassy. For Tabriz, the bubble volume fractions of 59 % of the heated plagioclase-hosted MI are superior to this threshold, going from 6 to 10 vol%, with two outliers at 24 and 26 vol% (**Supplementary Fig. 4**).

4.2. Heating experiments

Examples of MI before, during and after the heating experiments are shown in **Fig. 3** and **Supplementary Fig. 3**. Heating ramps for the plagioclase and clinopyroxene crystals are reported in **Table 2**. During the heating ramps, melting started around 1000-1060 °C for plagioclase-hosted MI from Alborz, while it began around 1090-1100 °C for the Tabriz ones (**Supplementary Table 1**). All plagioclase-hosted MI were homogenized at 1120 °C (**Supplementary Table 1**). During the experiments in clinopyroxenes, the visibility was not as good as in plagioclase crystals so the exact temperature of beginning of melting is generally not known. However, the MI were homogenized after being heated up to 1120 or 1160 °C for Alborz and Tabriz, respectively. In most cases, plagioclase-hosted MI showed a homogeneous silicate liquid plus a vapor bubble at the quenching temperatures (**Fig. 3a-g**). However, the bubbles did not dissolve in the MI, even at high temperature after melting of the daughter phases. For some clinopyroxene-hosted MI, the crystals did not dissolve into the melt with further heating, suggesting that these MI represent heterogeneous trapping of melt and minerals, and hence were not analyzed. These types of MI are classified in the literature as mixed inclusions (Roedder, 1979). 47 % of the observed MI showed a homogenous liquid phase at the temperature from which the MI was quenched (**Fig. 3h-k**). These MI that quenched to a homogeneous glass phase show a maximum size of 60 µm (**Fig. 3h-k**; **Supplementary Table 1**).

4.3. Major element compositions of MI

A total of 145 MI were brought to the surface of the crystals and the compositions of 56 of them were quantified using EMP (**Supplementary Tables 1-2**). The others MI were either too small, or fractured, or there was no room for analysis to avoid previous SIMS analyzed spots, or the crystals were lost during the sample preparation at the different steps.

For the Alborz region, the eleven unheated MI hosted in clinopyroxene show a trachytic composition, with the exception of one with a dacitic composition. The SiO_2 contents of these unheated MI vary from 63.5 to 66.1 wt% and their $Na_2O + K_2O$ contents between 11.2-12.2 wt% (**Fig. 2**). The eight heated MI in clinopyroxene also show trachytic compositions, apart from two MI presenting a dacitic affinity. In particular, SiO_2 varies from 61.4-65.8 wt% and $Na_2O + K_2O$ from 5.7-11.7 for heated MI (**Fig. 2**). For the 16 heated MI hosted in plagioclase, the MI compositions plot in the trachyandesitic field of the TAS diagram (**Fig. 2; Table 3**) (Le Bas et al., 1986). The SiO_2 contents of these heated MI vary from 54.6 to 59.2 wt% and their $Na_2O + K_2O$ contents between 8.0-9.8 wt% (**Fig. 2**). Three heated MI hosted in plagioclase lie on the boundary with the trachytic field (60.3-62.1 wt% SiO_2; 9-10 wt% $Na_2O + K_2O$) (**Fig. 2**). Most of the MI in heated plagioclase of both samples are in the same field as the whole rocks of the trachyandesites (**Fig. 2; Table 1**).

For Tabriz, the two unheated MI hosted in clinopyroxene show a slightly higher composition than the Alborz ones (67.6-67.8 wt% SiO_2; 12.2-12.4 wt% $Na_2O + K_2O$). One heated MI hosted in clinopyroxene shows a trachyandesitic composition (**Fig. 2**). The 18 heated MI hosted in plagioclase from Tabriz are similar in composition to those from Alborz described above. In fact, these MI show compositions between the trachyandesitic and trachytic fields (55.5-65.2 wt% SiO_2; 6.0-10.9 wt% $Na_2O + K_2O$) (**Fig. 2**).

In the Harker diagrams, all MI pertain to shoshonitic series, apart from three dacitic MI (including an unheated clinopyroxene-hosted MI and two heated ones, poor in K_2O) (**Fig. 4a**). One of the heated dacitic MI is likely to have been overheated, as it shows lower Na_2O and K_2O and Al_2O_3 concentrations and high FeO, MgO and CaO concentrations. However, the two other dacitic MI do not show anomalous compositions, so these MI could correspond to other melts trapped by the crystals. The Al_2O_3, CaO and FeO contents of the trachyandesitic MI are variable depending on the hosts (**Fig. 4b-d**). Heated MI in plagioclase from both regions have higher CaO, FeO and MgO contents compared to MI in clinopyroxene crystals (**Fig. 4c-d**). Whole rocks of the samples plot in the same field as the MI that have low SiO_2 contents (< 57 wt%) (**Fig. 4**), as in **Fig. 2**. For a given MgO value, SiO_2 of the whole rocks are lower than MI compositions (**Fig. 4e**), while K_2O of the whole rocks are higher than some compositions of heated MI in plagioclase but lower than the other clinopyroxene- and plagioclase-hosted MI compositions (**Fig. 4f**).

4.4. Compositions of host minerals

MI hosts crystals are plagioclase that are mainly bytownite while few of them are labradorite or anorthite, with Anorthite ($An = \frac{Ca}{Ca + Na + K}$) content of 73 ± 2 % for Alborz and slightly higher for Tabriz (78 ± 11 %). Clinopyroxene are augites, with a similar Enstatite content ($En = \frac{Mg}{Mg + Fe + Ca}$) of 42 ± 1 % or 41 ± 3 % for Alborz and Tabriz, respectively (**Supplementary Fig. 5; Supplementary Table 2**). Plagioclase crystals sometimes show some zonations while clinopyroxenes are mostly reverse-zoned, indicating changes in the magmatic storage conditions (Costa et al., 2020; Costa and Morgan, 2010; Petrone et al., 2016). The Mg number ($Mg\# = \frac{Mg}{Mg + Fe_{tot}}$) of the clinopyroxene host crystals from Alborz is nearly constant, from 0.67-0.70, indicating that MI were trapped at the same degree of magma differentiation (**Supplementary Fig. 6**). For Tabriz, the Mg# of two clinopyroxenes hosts is lower and is of 0.6 (**Supplementary Fig. 6**). For plagioclase, the anorthite content is more variable, with An values mainly between 70 and 74 % (**Supplementary Fig. 7**). Some MI hosted in plagioclase crystals show a high MgO and FeO content, in the An-rich host plagioclase (3-4 wt% in MgO, 10-13 wt% in FeO, for An82-92) (**Supplementary Fig. 7**).

4.5. Raman in bubble-bearing MI

As CO_2 is poorly affected by diffusion through the host mineral but much more by the formation of shrinkage bubbles (Metrich and Wallace, 2008; Portnyagin et al., 2008), the quantification of the amount of CO_2 in our bubble-bearing MI was carried out. 30 bubble-bearing MI analyzed by Raman showed characteristic peaks of CO_2 (**Methods; Supplementary Fig. 8**). However, signals were difficult to fit, because they either showed low intensity peaks with less than 3 points above the background or showed a peak asymmetry. Only one Raman signal in a bubble was successfully fitted, leading to a low CO_2 density of 0.05 $g.cm^{-3}$ (**Supplementary Fig. 8; Supplementary Table 1**) likely affected by a large error bar (Remigi et al., 2021). Using equation (1), and knowing the melt and bubble volumes [using Tucker et al. (2019)], the CO_2 content in this bubble is 198 ± 40 ppm (with a worst-case scenario error of 20%), representing 12% of the total CO_2 in the MI (see next section) (**Supplementary Fig. 8; Supplementary Table 1**). This bubble comprised 1 % of the host MI total volume (**Supplementary Fig. 8; Supplementary Table 1**).

4.6. Volatile content of the magma

35 MI were successfully analyzed for volatiles. For Alborz, 11 unheated MI in clinopyroxene, 4 heated MI hosted in clinopyroxene, and other 8 heated MI hosted in plagioclase were analyzed by SIMS. For Tabriz, one heated MI hosted in clinopyroxene and 11 heated MI hosted in plagioclase were analyzed by SIMS, to obtain a database of volatile contents of MI from these two Iranian localities (**Supplementary Tables 1-2**).

Volatile contents detected in MI in clinopyroxene and plagioclase are shown in **Fig. 5-6** and **Supplementary Fig. 9** (**Supplementary Table 2**). CO_2 contents are relatively high for the degree of differentiation that the studied MI represent. In particular, up to 6733 ppm of CO_2 was detected in a bubble-bearing MI hosted in plagioclase from Tabriz, with a bubble occupying 6 vol% of the MI (**Fig. 5a**; **Supplementary Table 2**). For unheated clinopyroxene-hosted MI from Alborz, CO_2 contents range from 326 (± 3) ppm to 4243 (± 42) ppm, with an average of 1827 ppm. In heated clinopyroxene crystals, CO_2 contents of MI range from 183 (± 2) ppm to 5272 (± 53) ppm. The values vary from 401 (± 4) ppm to 5668 (± 57) ppm (with an average of 2101 ppm) for heated plagioclase-hosted MI from Alborz, while for Tabriz, they are from 76 (± 1) to 6733 (± 67) ppm. The only clinopyroxene-hosted MI from Tabriz gives a value of 2703 ± 27 ppm.

Water contents in MI are variable for unheated clinopyroxene-hosted MI from Alborz, varying between 0.2 to 6.2 (± 0.1) wt%. Two different populations can be identified: one between 0.2 to 2 (± 0.04) wt% and another with higher contents: from 5 (± 0.1) to 6 (± 0.1) wt% (**Fig. 5b**; **Supplementary Table 2**). H_2O contents are very low for MI in heated crystals, as reported below (**Fig. 5b**; **Supplementary Table 2**).

In heated clinopyroxene crystals, H_2O range from 0.02 to 0.13 wt%, as well as in the heated plagioclase crystals from Alborz. In heated plagioclase crystals from Tabriz, H_2O contents are also significantly low, as 0.03 wt%, or under the detection limit.

By comparing the H_2O between unheated or heated crystals, some H may have been lost during the experiments, even if caution was taken during the experiments to not stay too long at high temperature (**Table 2**). However, as the H_2O data in heated clinopyroxene shows two different populations (one with a relatively low content and another one with higher values; **Supplementary Table 2**), no H_2O correction was applied to the heated minerals.

Fluorine contents in MI are higher in Alborz trachyandesite, compared to Tabriz ones (**Fig. 5c**; **Supplementary Table 2**). F is variable for unheated clinopyroxene-hosted MI from Alborz, between 167 (± 3) and 972 (± 19) ppm (with an average of 506 ppm). In heated clinopyroxene crystals, concentrations of F range from 795 (± 16) to 1146 (± 23) ppm (with an average of 971 ppm). In heated plagioclase crystals, F is from 23 to 432 ppm (with an average of 238 ppm). For Tabriz for MI in plagioclase, F is from 13 to 164 ppm. F contents of MI hosted in clinopyroxene and some plagioclase crystals from Tabriz were under the detection limit of SIMS.

Sulfur contents in MI are relatively low for clinopyroxenes but higher for plagioclase from both the Alborz and the Tabriz areas (**Fig. 5d**; **Supplementary Table 2**). For unheated clinopyroxene-hosted MI from Alborz, S is between 48 and 172 ppm (with an average of 89 ppm). For MI hosted in heated clinopyroxene crystals from Alborz, S detected values range from 2 to 156 ppm (with an average of 83 ppm). In heated plagioclase crystals from Alborz, the sulfur in MI is from 59 to 327 ppm, with a high value of 2347 ppm. For Tabriz in MI from plagioclase, S is in the same range as for Alborz, from 14 to 2953 ppm (with an average of

1264 ppm). S content of one clinopyroxene-hosted MI from Tabriz was under the detection limit.

For Chlorine, concentrations are higher in plagioclase-hosted heated MI from Alborz and Tabriz than in clinopyroxenes (**Fig. 5e**; **Supplementary Table 2**). For unheated clinopyroxene-hosted MI from Alborz, Cl is between 231 (± 7) and 852 (± 26) ppm (with an average of 592 ppm). In heated clinopyroxene crystals, Cl detected values range from 550 (± 17) to 595 (± 18) ppm (with an average of 573 ppm). In heated plagioclase crystals, Cl contents are from 49 to 1334 ppm (with an average of 831 ppm). For Tabriz heated plagioclase MI, Cl contents are from 36 to 2953 ppm (with an average of 1264 ppm). Cl was below detection limit in the clinopyroxene-hosted MI from Tabriz.

Halogen ratios, such as Cl/F, can be specific tracers of the origin of magmas, magma storage conditions or eruption dynamic (Balcone-Boissard et al., 2023) (**Supplementary Fig. 9; Supplementary Table 1**). A linear correlation is identified for MI in heated plagioclase and unheated clinopyroxene crystals from Alborz (**Supplementary Fig. 9; Supplementary Table 1**), with Cl/F ratios between 1 and 3 for clinopyroxene or 1 and 4 for heated plagioclase, with two higher values of 12 and 48. Such correlation indicates a common magma source. For Tabriz, the data is too scarce to be able to conclude on the source but they show two high ratios of 59 and 175. For Cl versus CO_2, Cl values seem to be constant while CO_2 varies (**Fig. 6b**). No correlation seems to have been identified for S or F versus CO_2 (**Fig. 6c,d**). Cl versus F shows a Cl-enrichment, as in other volcanic arcs (**Supplementary Fig. 9**) (Rose-Koga et al., 2014).

Volatiles and K_2O contents are variable for plagioclase and clinopyroxene MI (**Supplementary Fig. 10**). TiO_2 contents are constant for all volatiles for unheated clinopyroxenes (**Supplementary Fig. 10**). For plagioclase, TiO_2 contents are variable depending on the volatiles (**Supplementary Fig. 10**). SiO_2 contents for plagioclase MI are in the same ranges, mainly from 54 to 59 wt% SiO_2, while volatile contents are spread out. SiO_2 values for unheated clinopyroxene are also in the same range, from 64 to 68 wt% SiO_2 but their volatile contents are dispersed (**Supplementary Fig. 10**).

4.7. Estimates of magma storage temperatures and pressures

For silicic melts, volatile saturation in melts is strongly controlled by pressure and significantly less so by temperature and melt composition (Wallace et al., 1999), which allows to retrieve pressures and depths of magmas based on MI volatiles concentrations.

The pre-eruptive magma storage temperatures using the clinopyroxene-liquid thermometer for Alborz give lower temperatures for MI in unheated crystals compared to heated clinopyroxene (859 ± 39 °C and 988 ± 58 °C, respectively) (**Supplementary Fig. 11**; **Supplementary Table 3**) (Putirka, 2008). No temperature was calculated for MI in heated cpx of Tabriz (lack of data). For plagioclase-hosted heated MI, the estimated temperatures were calculated using the plagioclase-liquid thermometer (Putirka, 2008) and are of the same order of magnitude for Alborz and Tabriz (1083 ± 11 °C and 1087 ± 24 °C, respectively) (**Supplementary Fig. 11**; **Supplementary Table 3**). Temperatures calculated for MI of Alborz using the clinopyroxene-liquid geothermobarometer of Masotta et al. (2013) are higher compared to the ones calculated with Putirka (2008) (**Supplementary Fig. 11, Supplementary Table 4**). In fact, the temperatures estimates for Alborz are 1010 ± 22 °C for unheated MI in clinopyroxene and 1022 ± 47 °C for heated MI in clinopyroxene (**Supplementary Fig. 11, Supplementary Table 4**).

Most of the studies are focused on the reconstruction of H_2O and CO_2 because they allow to calculate the pressure of entrapment of MI if we assume that the magma was at the H_2O-CO_2 saturation (Newman and Lowenstern, 2002). For both Alborz and Tabriz, nine pressures were calculated for MI using MagmaSat calculations (Ghiorso and Gualda, 2015). These pressures are mostly ranging from 60 to 310 MPa for all crystals. Few outliers either show very high pressures, with three pressures higher than 900 MPa (**Supplementary Fig. 11, Supplementary Table 3**). Assuming a magma density of 2.3 $g.cm^{-3}$ (Carr and Gazel, 2017), the pressure range given by the MI (60-310 MPa) correspond to 3-14 km in depth. Nevertheless, the MI having H_2O-CO_2 contents indicating high storage pressures of 956, 1065 MPa and even 1451 MPa correspond to entrapment depths of 42-64 km (**Supplementary Fig. 11, Supplementary Table 4**).

Using the clinopyroxene-liquid geothermobarometer of Masotta et al. (2013), calculated pressures show a good overlap relative to those calculated based on MagmaSat. For instance, for unheated clinopyroxene MI from Alborz, pressures based on clinopyroxene and MI compositions are 150 ± 65 MPa, while they are 194 ± 55 MPa for heated clinopyroxene MI from Alborz (**Supplementary Fig. 11, Supplementary Table 4**). The corresponding depths of these ranges of pressures (93-297 MPa) range from 4 to 13 km depth, assuming a magma density of 2.3 $g.cm^{-3}$ (Carr and Gazel, 2017). These depths are in the same order of magnitude of pressure of the main range determined by MagmaSat.

5. Discussion

5.1. Petrological implications of the volatile analyses

The volatile measurements in the MI of the Eocene Iranian volcanics allow us to estimate the pre-eruptive CO_2 content of these magmas. As some MI are bubble-bearing, the representativity of the CO_2 analyses in the glass needs to be assessed. The MI compositions can be modified by post-entrapment processes and re-equilibration of fast-diffusing elements such as H if the magma was stored for an extended period of time (Bucholz et al., 2013; Gaetani et al., 2012; Portnyagin et al., 2008; Wallace et al., 2021). Regarding C, the CO_2 content can be re-distributed in bubbles in the MI, if bubbles are formed during post-entrapment crystallization (Steele-Macinnis et al., 2011) or as shrinkage bubbles in response to cooling (Lowenstern, 1995; Metrich and Wallace, 2008; Roedder, 1979). Some studies assess the CO_2 concentrations by summation of the CO_2 contents of the glass determined by SIMS and the CO_2 contained in the bubble(s) (Esposito et al., 2011; Hartley et al., 2014; Metrich and Wallace, 2008; Tucker et al., 2019). According to our Raman analyses, bubbles in bubble-bearing MI showed the presence of CO_2 but with very low densities (**Supplementary Fig. 8; Supplementary Table 1**). Considering only the MI where the CO_2 in the bubble was satisfyingly quantified, we found ~198 ppm of CO_2 in the bubble (**Supplementary Fig. 8; Supplementary Table 1**). As the bubble represents ~1 % of the total volume of the MI and as the CO_2 concentration in the glass was 1438 ppm, the bubble may contain ~12 % of the total CO_2 in the inclusion (**Supplementary Table 1**). This percentage is low considering that bubbles can contain up to 90 % of the total CO_2 of MI (Esposito et al., 2011; Hartley et al., 2014; Moore et al., 2015). Therefore, the combination of weak Raman CO_2 signals, low bubble CO_2 density, and generally low bubble volume percentages, suggests that MI need limited correction for CO_2 content lost in the bubble. Assuming that these measurements are representative of our bubble-bearing MI set, MI CO_2 contents could be corrected by adding 12

% to the measured values. However, in this study, we dismissed this correction as the potential 12 % value is based on only one MI out of 35. SIMS-MI CO_2 values were thus not corrected to avoid introducing bias and produce conservative, but reliable, measurements, thus representing minimum values.

The volatile content further provides important information on melt storage pressures, fostering our understanding of the plumbing system and degassing behavior of the Iranian magmas. Considering the barometer using H_2O and CO_2 contents of the MI (MagmaSat) or clinopyroxene compositions and H_2O contents (Masotta et al., 2013), magmas were stored at a wide range of pressures, mainly corresponding to depths between 3 and 14 km. A trans-crustal magmatic plumbing system with various storage depths is involved, in accordance with the wide range of pressures obtained (60-310 MPa). These pressure estimates can be affected by secondary processes such as H_2O loss (or gain) due to diffusion at high temperature after MI formation. This can occur either before eruption during shallow crustal melt storage, or during deposition after eruption, or during high-temperature heating experiments (Bucholz et al., 2013; Esposito et al., 2023; Gaetani et al., 2012; Portnyagin et al., 2008; Wallace et al., 2021). While the former two processes are difficult to estimate for MI hosted in plagioclase and clinopyroxene crystals, the latter process was mitigated by short experiment duration from 2 to 3 hours and relatively short time spent at high temperatures, between 15-20 min above 1100 °C (**Table 2**). The combination of low H_2O and high CO_2 concentrations and, thus, low $\frac{H_20}{H_20 + CO_2}$ ratios in silicate melts may indicate an external income of CO_2 from deeper levels within the magma plumbing system, driving melt dehydration and crystallization at shallower levels (CO_2 flushing) (Caricchi et al., 2018). However, K_2O MI concentrations are higher for low An# plagioclase, and are uncorrelated to CO_2 concentrations, whereas a correlation between K_2O content of the MI and CO_2 is expected if CO_2 flushing occurs (**Supplementary Fig. 7a; 10b1**) (Caricchi et al., 2018). Thus, our MI may not be representative of CO_2 flushing. As previously discussed (**Fig. 6a**), the lack of correlation between CO_2 in MI with An# or Mg# of the host minerals for Alborz or Tabriz MI (**Supplementary Fig. 12**) may further indicate that water loss should be ascribed to other primary/secondary processes, the recognition of which is beyond the scope of this study. Thus, our pressure estimates derived from H_2O and CO_2 contents are considered here as minimum values. Independent of the accuracy of the magma crystallization depths, the total CO_2 concentration of studied MI is not affected by the H-loss by diffusion, with the assumption that the MI were originally trapped as a single homogeneous silicate liquid phases.

Plagioclase crystals in both samples crystallize at a relatively earlier stage of differentiation compared to clinopyroxene crystals, as shown on the SiO_2 vs MgO diagram, as SiO_2 concentrations are lower for relatively higher MgO contents (**Fig. 4e**). In general, MI and their hosts composition show a reasonably good correlation compatible with simple crystal fractionation (**Supplementary Fig. 6-7**). Considering these two points, plagioclase crystals may have crystallized earlier than clinopyroxene. Furthermore, Rhyolite-MELTS runs carried out using a trachyandesitic initial melt composition from our MI set (PS2-FD1-2-Z8-MI8) allow to model the liquid line of descent of the system, with isobaric conditions (310 MPa; pressure of the MI of interest), varying T (**Fig. 2**) and without considering CO_2 (Ghiorso and Gualda, 2015; Gualda et al., 2012) (**Supplementary Table 5**). Oxygen fugacity has been either set without a buffer or the NNO or QFM buffers but the oxidation state does not appear to significantly influence the results. The modelled liquid lines of descent show an evolution

consistent with the whole-rocks and the MI compositions hosted both in plagioclase and clinopyroxene (**Fig. 2**). A kink in the curves is observed in trachytic compositions, where Na increases in plagioclase crystals. Clinopyroxene compositions change from En_{58-60} to En_{38-41} at a temperature around ~1050 °C, and are comparable to the ones investigated here. The liquid then evolves to rhyolitic composition with decreasing temperature (up to ~880 °C). The predicted order of appearance of mineral phases is in good agreement with the MI compositions and the compositions of the hosts, especially for clinopyroxene (**Fig. 2**). These Rhyolite-MELTS runs are also in favor of the crystallization of plagioclase before the low-En clinopyroxene. Plagioclase crystals could thus have trapped a trachyandesitic liquid, while fractional crystallization led to clinopyroxene trapping trachytic, more evolved melts.

5.2. CO_2 budget of ascending melts and climatic implications

5.2.1. Assessment of the primary CO_2 budget

The CO_2 measured in MI from Alborz and Tabriz is similar for heated and unheated crystals (**Fig. 5;** overlapping errors bars in **Fig. 7; Supplementary Fig. 13; Supplementary Table 1**). Therefore, the CO_2 budget of ascending melts recorded in plagioclase- and clinopyroxene-hosted MI can be assessed by considering all CO_2 values as a unique range, with the minimum, maximum and average values of all CO_2 contents in these MI that are 76, 6733, and 1757 ppm, respectively (**Fig. 7; Table 4**).

It is important to keep in mind, however, that the maximum CO_2 value of MI using SIMS is a minimum estimate of the pre-eruptive degassed CO_2 of ascending melts since additional CO_2 may have been lost during the ascending path of the magma from the source to the lower crust. The volume of middle-late Eocene (~45-36 Ma) Iranian volcanics were quantified between 7.6×10^4 and 3.8×10^5 km^3 (van der Boon et al., 2021), based on a compilation of available geological maps (Sahandi et al., 2014) and assuming thicknesses between 2 and 10 km of volcanic formations from the literature (Berberian and King, 1981; Morley et al., 2009; Stöcklin, 1974; van der Boon et al., 2021, and references therein; Verdel et al., 2011). To the best of our knowledge, the Central Eocene volcanics that are buried beneath a few-km-thick sequence of Oligo-Miocene sediments were not included in these calculations, as only outcropping volcanics were considered. The volumes estimates mentioned above should thus be considered as minimum values. To estimate the outflux of CO_2, f_{CO_2}, from the SIMS measurements, the following equation was used (2):

$$f_{CO_2} = \frac{C_{CO_{2,\ SIMS}} * m_T}{t} \#(2)$$

where $C_{CO_{2,\ SIMS}}$ is the CO_2 content of MI measured with SIMS, m_T is the total mass of parental magma in tons (t) and t is the duration of the eruptive event in years.

Assuming an average density of the magma of 2.32 g cm^{-3} (using the Igpet software; Carr and Gazel, 2017) and referring to the magma volumes estimated by van der Boon et al. (2021), the minimum and maximum mass erupted during the middle Eocene are $2\text{-}9\times10^{14}$ t (**Table 4**). Considering 70 % of magma crystallization to form a trachyte from a basalt (Macdonald et al., 2008), the range of total mass of parental magma would be 3×10^{14}-1.5×10^{15} t. The main source

of uncertainty in the CO_2 outflux comes from the magma volume estimates. We overcome this limitation by accounting for the minimum and maximum values of the magma volume estimated from van der Boon et al. (2021). (1) Accounting for the estimated pre-eruptive CO_2 budget of magmas as derived from the CO_2 concentrations of MI (76-6733 ppm) and the minimum estimate of the total mass of Iran parental magma from 45-36 Ma (3×10^{14} t), the outflux of CO_2 during this period is of 0.003-0.22 Mt CO_2/yr (**Table 4**). This CO_2 flux corresponds to a total CO_2 emission of 2.28×10^{16}-2.02×10^{18} g CO_2 (**Table 4**). Converting our CO_2 flux in carbon (C), the C flux would be of ~0.001-0.061 Mt C/yr, corresponding to a total C emission of 6.22×10^{15} -5.51×10^{17} g C during the middle-late Eocene (~6-551 Pg C) (**Fig. 8; Table 4; Supplementary Table 1**). (2) Accounting for the estimated pre-eruptive CO_2 budget of magmas as derived from the CO_2 concentrations of MI (76-6733 ppm) and the maximum estimate of the total mass of Iran parental magma from 45-36 Ma (1.5×10^{15} t), the outflux of CO_2 during this period is of 0.01-1.12 Mt CO_2/yr (**Table 4**). This CO_2 flux corresponds to a total CO_2 emission of 1.14×10^{17}-1.01×10^{19} g CO_2 (**Table 4**). Converting our CO_2 flux in carbon (C), the C flux would be of 0.003-0.306 Mt C/yr, corresponding to a total C emission of 3.11×10^{16} -2.75×10^{18} g C during the middle-late Eocene (~31-2800 Pg C) (**Fig. 8; Table 4; Supplementary Table 1**). The relative uncertainty on the outflux of CO_2 is 4 %, based on the propagation of measurement uncertainty of CO_2 by SIMS and the age uncertainties reported by van der Boon et al. (2021). Since our CO_2 SIMS measurements are likely to underestimate the true CO_2 content of Iranian magmas, we can consider estimates calculated with the highest CO_2 measured concentration by SIMS (6733 ppm of CO_2): 0.061-0.306 Mt C/yr (551-2800 Pg C). Following our pressure and temperature estimates, and CO_2 degassing budget, a schematic crustal section of the Iran Alborz and Tabriz magmas is shown on **Fig. 8**.

5.2.2. Assessment of possible CO_2 degassing from intruded carbonate rocks

The amount of C released during volcanic episodes increases substantially when eruptions occur within carbonate-rich rocks due to contact metamorphism of carbonates, as well as CO_2 released by magmatic assimilation of carbonates (Aiuppa et al., 2017; Deegan et al., 2010; Iacono-Marziano et al., 2009; Lee et al., 2013; Lee and Lackey, 2015). However, the fraction of CO_2 released by magmatic assimilation of carbonates is not constrained for Iran. Furthermore, most of the MI studied here record depths which are deeper than those of the Meso-Paleozoic sedimentary carbonate sequence below those two studied localities in Iran (~1.5 km and ~9-11 km) (Allen et al., 2003; Geological Survey and Mineral Exploration of Iran, 2006, 1995; Madanipour et al., 2018). Therefore, the CO_2 of most studied MI is likely to be of magmatic origins. Van der Boon et al. (2021) and Zhang et al. (2023) used a range of "limestone factors" to calculate the whole amount of CO_2 released during Eocene volcanic episodes of Iran and Tibet, respectively. Limestone factors involving 3.6–8.6 times higher CO_2 release by volcanic outgassing alone were constrained based on estimates of the CO_2 released from carbonate sediments during the emplacement of the Emeishan large igneous province (China) in the end-Guadalupian (Courtillot and Renne, 2003; Ganino and Arndt, 2009; Self et al., 2006). As these limestone factors were estimated based on a Large Igneous Province in China, which does not necessarily correspond to our geological context, we preferred not to use them to calculate the final C flux. However, it is important to keep in mind that Eocene volcanism in Iran erupted in shallow marine basins and through carbonate-rich rocks (Berberian and King, 1981). Were therefore warn the reader that the CO_2 outgassing due to

Iranian magmatism could be up to about one order of magnitude larger than values provided above (0.061-0.306 Mt C/yr).

5.2.3. Contribution of Iranian magmatism to the MECO

The MECO is accompanied by a rise in atmospheric CO_2 concentrations (Bijl et al., 2010; Henehan et al., 2020; Judd et al., 2024; Ma et al., 2024), warming in surface and intermediate deep-water, extensive deep-sea carbonate dissolution (Bohaty et al., 2009) and marine biotic change (Bijl et al., 2010; Cramwinckel et al., 2019; Edgar et al., 2013; Witkowski et al., 2012). Sluijs et al. (2013) and van der Ploeg (2018) showed, with reconstructions and simulations of the carbon cycle, an imbalance in the long-term inorganic carbon cycle which is likely to have been caused by enhanced volcanism and a decrease in continental silicate weathering during the MECO, in contrast to expectations from the silicate weathering thermostat hypothesis. Indeed, van der Ploeg et al. (2018) surmised, based on osmium isotope records and carbon and osmium cycle modeling, that global early and middle Eocene warmth gradually diminished the weatherability of continental rocks and the strength of the silicate weathering feedback, leading to the prolonged accumulation of volcanic CO_2 in the oceans and atmosphere during the MECO. Foraminifera boron isotope ratios and carbon cycle simulations constrained by available proxy data led to estimates of the carbon cycle imbalance during the MECO around 2×10^{18} g C to 4×10^{18} g C (2000-4000 Pg C) (Henehan et al., 2020; Sluijs et al., 2013; van der Boon et al., 2021; van der Ploeg et al., 2018).

New ages of Iranian Eocene volcanics provided by van der Boon et al. (2021) and previously published radiometric ages showed that many volcanic areas in Iran were active simultaneously around 40 Ma (with a clustering of ages during the middle Eocene). The MECO thus corresponds to a phase of intense volcanism in this area, even if the uncertainty in the individual samples ages is larger than the duration of the MECO (van der Boon et al., 2021). Van der Boon et al. (2021) have taken the Deccan traps as a term of comparison as CO_2 degassing rates for continental arcs may be similar to (Marty and Tolstikhin, 1998) or larger than for continental flood basalts (McKenzie et al., 2016; Wignall et al., 2009). These authors calculated the amount of CO_2 degassed from these magmas based on a relationship between lava volume and CO_2 emitted during the emplacement of the Deccan Traps (Tobin et al., 2017), as no constraints on CO_2 emissions from these Iranian magmas existed so far. From this method, the minimum estimate for C released from middle Eocene volcanism in Iran ranges between 292-1461 Pg C (van der Boon et al., 2021). These C estimates increase to 1052-12565 Pg C considering the possible "limestone factor" (Berberian and King, 1981; Ganino and Arndt, 2009; van der Boon et al., 2021). Our C estimates derived from MI analyses (551-2800 Pg C) are within the range and even slightly higher than the total magmatic C estimate by van der Boon et al. (2021) or in their low range of the total C outgassed considering carbonates. Furthermore, our C total estimates are also in the range of the carbon anomaly that drives the MECO in carbon cycle simulations constrained by available proxy data (2000-4000 Pg C) (Henehan et al., 2020; Sluijs et al., 2013; van der Boon et al., 2021; van der Ploeg et al., 2018), and consistent with enhanced volcanism from the Azerbaijan-Bazman arc contributing to the MECO (Ma et al., 2024).

Plate boundary evolution and carbon fluxes models have been used to estimate a net C outgassing of ~46 Mt C/yr at around 40 Ma (Wong et al., 2019), whereas proxy data (e.g. CO_2 from leaf stomata, pedogenic carbonate $\delta^{13}C$, boron isotopes in foraminifera) suggest

significantly lower values of ~4.5 Mt C/yr (Foster et al., 2017). Considering that our maximum estimate of degassing flux from the Iranian magmas (0.3 Mt C/yr) could be one order of magnitude higher due to the limestone contribution, Iranian flare up emissions could account for ~6-60 % of the estimated net C outgassing. Apart from the Iranian flare-up, other magmatic events have occurred in the middle Eocene: (i) large volumes of magmas were erupted from multiple volcanic centers in the Basin and Range (Gans et al., 1989), (ii) increased arc volcanism around the Pacific rim, with the ignimbrite flare-up in the Sierra Madre Occidental of Mexico, (iii) an episode of magmatism in the East African Rift zone, as well as (iv) mid-ocean ridge volcanism in the North Atlantic (Ma et al., 2024; van der Ploeg et al., 2018, and references therein). While these magmatic events and associated degassing likely affected the overall atmospheric C budget, their timing and magnitude are presently not sufficiently well resolved to be linked with the MECO (van der Ploeg et al., 2018). The upper limit of ~60 % contribution due to C outgassing from Iranian magmas around 40 Ma seem relatively high. However, considering the length of the Neo-Tethyan subduction along the Arabian margin with respect to the global arc and mid oceanic ridges length in the middle Eocene, even a contribution of ~6% is significant. We emphasize that our C emission estimates are conservative, as CO_2-saturated magmas could have contained more CO_2 and could have been stored deeper than the storage depth of the targeted MI. We thus provide strong observational evidence in support of a major contribution to the MECO from Iranian magmatic flare up and degassing. We further stress that petrological quantifications of the volatile budget of magmas from arc settings are critical to improve estimates of magmatic CO_2 emissions and assess the possible climatic effects of volcanic degassing. Once sufficient data will be collected, these CO_2 estimates could even be used to constrain climate and/or carbon outflux models and improve understanding of past climate drivers and dynamics (Arndt et al., 2011; Castrogiovanni et al., 2024; Donnadieu et al., 2006; Lefebvre et al., 2013).

5. Conclusions

We provide the first quantification of the volatile content of unheated and heated MI in clinopyroxene and plagioclase from Eocene Iran trachyandesites. Our study shows that the MI are CO_2-rich and derive from trachyandesitic to trachytic melts. These data allow us to provide the first observation-based estimates of the amount of CO_2 degassed during the regional middle-late Eocene magmatic flareup, which range between 2.28×10^{16}-1.01×10^{19} g CO_2 and thus 6.22×10^{15}-2.75×10^{18} g C. Taking the maximum CO_2 concentration from SIMS measurements, the estimated total C outflux is 0.061-0.306 Mt C/yr and could be up to an order of magnitude higher considering the likely limestone contribution from interactions between magmas and carbonate-rich rocks. This degassed CO_2 from Iran is likely to have provided a significant contribution to the Middle Eocene Climatic Optimum. Future MI-based estimates of CO_2 degassing and better constraints on the magma volumes will enable us to improve the quantification of the magmatic contributions of Neo-Tethyan magmas to the MECO and, possibly, other long-term Cenozoic climate trends.

Acknowledgments

E. Haghfarshy and N. Qavim are highly thanked for providing the samples. L. Ostorero would like to thank R. Marchesi for his precious help with thin section preparation and also L. Galimberti and F. Vergani for their help in the laboratory. We also thank S. Favaro for helping

crushing the samples, M. Barbarano and A. Resentini for sample preparation and Frantz magnetic separation as well as M. Papetti and K. El Belashouni for their significant help during their bachelor internship. Regarding the analyses, we thank the LG-SIMS-Nancy team for their help with the Indium mount preparation and for the SIMS volatile analyses. We are also grateful to Petrolab (Sardegna) for thin section preparations, to Bureau Veritas Mineral Laboratories (Canada) for whole rock analyses, to P. Gentile for SEM imaging and A. Risplendente for the EMP analyses. Raman facilities were provided by the University of Milano-Bicocca and microthermometric facilities were provided by the Department of Earth and Environmental Sciences (DISAT). We also thank M. Ghiorso and T. Pereira for their help with Rhyolite-MELTS. P. Sternai thanks the International Lithosphere Program and the Young Academy of Europe. Funding: L. Ostorero benefited from a travel grant from the 2023 Europlanet Expert Exchange Programme to go to Nancy in 2023. This work has been supported by Fondazione Cariplo and Fondazione CDP (Grant n° 2022- 1546_001), by the Italian Ministry of Education, MUR (Project Dipartimenti di Eccellenza, TECLA, Department of Earth and Environmental Sciences, University of Milano-Bicocca), and by the Alexander von Humboldt Foundation (research project CEMENT, P.I.: P. Sternai). P. Bouilhol thanks Lorraine University of Excellence for funding Ephemeris Impact Project. This is Ephemeris contribution #01. PRIN2022 “CRUStal CArbon: exploring the role of the crust in the C cycle (CRUSCA)” (project n°2022HA8XCS) is also acknowledged by M.L. Frezzotti and R. Esposito.

Author contributions

PBa provided the Iran samples. Conceptualization: PS, PBo, RE; Data curation: LO; Formal analysis: LO; Funding acquisition: PS, PBo, MLF; Investigation: LO; Methodology: PS, RE, LO, PBo, VAM; Resources, supervision and validation: PS, RE, PBo, PBa; Visualization: LO; Writing of the original draft: LO; Reviews and editing: all authors.

Statements and declarations

Competing interests: All the authors declare no competing interests.

Data Availability

All data generated or analyzed during this study are included in this manuscript (and its supplementary information files).

Figure captions (colors should be used for all the figures in print)

Figure 1: Maps of Iran. (a) Digital elevation map of the study region with sampling sites in the regions of Tabriz and the Alborz mountains are shown, as well as the distribution of Eocene volcanic rocks after previous maps (Agard et al., 2011; Allen and Armstrong, 2008; Nalivkin, 1976; van der Boon et al., 2017); **(b)** Topography of Iran showing the main Zagros reverse fault, which is interpreted to coincide with the Arabian-Iranian suture zone (Ballato et al., 2013). In **(a-b)**, a global topography Digital Elevation Model was used. "UDMA" refers to the Urumieh–Dokhtar Magmatic Arc and "Mtns" refers to Mountains.

Figure 2: Total Alkali Silica (TAS) diagram (Le Bas et al., 1986) **of unheated and heated clinopyroxene and plagioclase-hosted melt inclusions (MI) from Alborz and Tabriz (Iran), as well as liquid compositions predicted by Rhyolite-MELTS.** Whole-rocks of the samples are also shown. Melt inclusions literature data from Iran are also shown for comparison, such as the olivine-hosted MI of the Pliocene-Quaternary lavas from the Qorveh-Bijar volcanic belt (Salehi et al., 2020). Whole rocks from Alborz basalts and phonotephrite are also shown (Verdel et al., 2011), as well as the host rocks of the olivine-hosted MI from Salehi et al. (2020). For Rhyolite-MELTS predictions (Ghiorso and Gualda, 2015; Gualda et al., 2012), the composition of a trachyandesitic MI (PS2-FD1-2-Z8-MI8) was used with an isobaric run (at 310 MPa, found for this specific MI), with a varying temperature (from the liquidus temperature to ~880 °C) with different oxidizing conditions (no buffer, NNO and QFM). The appearance and disappearance of orthopyroxene ("opx"), clinopyroxene ("cpx"), plagioclase ("plag") and K-feldspar at low temperature (sanidine, "san") predicted by Rhyolite-MELTS are highlighted.

Figure 3: Photomicrographs of MI as found in plagioclase and clinopyroxene crystals before heating experiments, during and after heating. **a-g)** Partially crystallized melt inclusion in a plagioclase, from ambient temperature **(a)** to complete homogenization **(f)** and after quenching **(g)**. **h-k)** Melt inclusions in clinopyroxene crystals, before the experiment and after quenching. No pictures from the experiments are shown because the visibility was low.

Figure 4: Harker diagrams for unheated and heated clinopyroxene- and plagioclase-hosted MI. a) K_2O vs SiO_2; **b)** Al_2O_3 vs SiO_2; **c)** CaO vs SiO_2 and **d)** FeO vs SiO_2. Whole-rocks are also shown.

Figure 5: Volatile contents depending on the MI hosts in trachyandesites from Alborz or Tabriz (unheated or heated clinopyroxene and plagioclase crystals). a) CO_2 contents in MI, depending on the host and sample; **b)** H_2O; **c)** F; **d)** S; **e)** Cl. The error bars on SIMS measurements are lower than the symbols.

Figure 6: Volatile content from SIMS of unheated and heated MI hosted in clinopyroxene and plagioclase crystals from Alborz and Tabriz. a) CO_2 and H_2O contents in MI; **b)** Cl versus CO_2 concentrations in MI; **c)** S versus CO_2 concentrations in MI; **d)** F versus C_2O concentrations in MI. Error bars correspond to SIMS uncertainties. The error bars on SIMS measurements are lower than the symbols.

Figure 7: Whisker plot of the CO_2 contents in unheated or heated clinopyroxene and plagioclase crystals. The center line denotes the median value (50th percentile), while the box contains the 25th to 75th percentiles of the dataset. The black whiskers mark the 5th

and 95th percentiles, and values beyond these upper and lower bounds are considered outliers, marked with empty dots.

Figure 8: Simplified schematic crustal section of the Iran Alborz and Tabriz magmas and CO_2 degassing flux estimates during the middle-late Eocene. Supposing volatile saturation in Iran magmas considering the wide range of CO_2 concentrations, H_2O and CO_2 contents were considered as representative of the Iran magmatic pressures, temperatures and depths at Eocene times. The CO_2 flux range presented in this figure was calculated with the maximum CO_2 concentration measured by SIMS in the MI (see discussion; Table 4). The estimation of the thickness of the carbonate rocks (~1.5 km and deeper strata of unknown accurate thickness and depth) (Allen et al., 2003; Geological Survey and Mineral Exploration of Iran, 2006, 1995; Madanipour et al., 2018) **as well as Moho depth estimates are from present time in Tabriz and Alborz region. The Moho depth estimate is from a comparison between gravimetric Moho solutions and existing regional seismic studies: 50 ± 2 km** (Ebadi et al., 2019)**.** In the Eocene, the substratum had already undergone several phases of deformation; thus, for simplicity, strata are depicted here as sub-horizontal (Madanipour et al., 2018).

Tables captions

Table 1: Description of the samples from Iran studied here (location, coordinates (in the World Geodetic System WGS84) and nature of the samples are specified).

Table 2: **Heating ramps used for experiments on crystals from Iran. The durations of maintaining the temperature constant after each temperature step are also specified.**

Table 3: **Whole rock major and trace elements of the Iranian samples from Alborz and Tabriz. The sampling locations are specified in Table 1. Analyses have been performed at Bureau Veritas Mineral Laboratories (Canada) by ICP-OES (Inductively Coupled Plasma-Optical Emission Spectrometry). The type of deposit is specified. Data are expressed with total Fe as Fe^{3+} with LOI detailed.**

Table 4: Magmatic CO_2 flux mass balance calculations for Iran magmas assuming CO_2 concentrations of MI by SIMS. CO_2 values could be higher considering CO_2 released from carbonate sediments.

References

Agard, P., Omrani, J., Jolivet, L., Mouthereau, F., 2005. Convergence history across Zagros (Iran): constraints from collisional and earlier deformation. Int. J. Earth Sci. 94, 401–419. https://doi.org/10.1007/s00531-005-0481-4

Agard, P., Omrani, J., Jolivet, L., Whitechurch, H., Vrielynck, B., Spakman, W., Monié, P., Meyer, B., Wortel, R., 2011. Zagros orogeny: a subduction-dominated process. Geol. Mag. 148, 692–725. https://doi.org/10.1017/S001675681100046X

Aiuppa, A., Fischer, T.P., Plank, T., Robidoux, P., Di Napoli, R., 2017. Along-arc, inter-arc and arc-to-arc variations in volcanic gas CO 2 /S T ratios reveal dual source of carbon in arc volcanism. Earth-Science Rev. 168, 24–47. https://doi.org/10.1016/j.earscirev.2017.03.005

Alavi, M., 1994. Tectonics of the zagros orogenic belt of iran: new data and interpretations. Tectonophysics 229, 211–238. https://doi.org/10.1016/0040-1951(94)90030-2

Allen, M.., Ghassemi, M.., Shahrabi, M., Qorashi, M., 2003. Accommodation of late Cenozoic oblique shortening in the Alborz range, northern Iran. J. Struct. Geol. 25, 659–672. https://doi.org/10.1016/S0191-8141(02)00064-0

Allen, M.B., Armstrong, H.A., 2008. Arabia–Eurasia collision and the forcing of mid-Cenozoic global cooling. Palaeogeogr. Palaeoclimatol. Palaeoecol. 265, 52–58. https://doi.org/10.1016/j.palaeo.2008.04.021

Alpaslan, M., Frei, R., Boztug, D., Kurt, M.A., Temel, A., 2004. Geochemical and Pb-Sr-Nd Isotopic Constraints Indicating an Enriched-Mantle Source for Late Cretaceous to Early Tertiary Volcanism, Central Anatolia, Turkey. Int. Geol. Rev. 46, 1022–1041. https://doi.org/10.2747/0020-6814.46.11.1022

Amidi, S.M., Emami, M.H., Michel, R., 1984. Alkaline character of Eocene volcanism in the middle part of central Iran and its geodynamic situation. Geol. Rundschau 73, 917–932. https://doi.org/10.1007/BF01820882

Amidi, S.M., Michel, R., 1985. Cenozoic magmatism of the Surk area (central Iran) stratigraphy, petrography, geochemistry and their geodynamic implications. Géologie Alp. 61, 1–16.

Arndt, S., Regnier, P., Goddéris, Y., Donnadieu, Y., 2011. GEOCLIM reloaded (v 1.0): a new coupled earth system model for past climate change. Geosci. Model Dev. 4, 451–481. https://doi.org/10.5194/gmd-4-451-2011

Arslan, M., Aslan, Z., 2006. Mineralogy, petrography and whole-rock geochemistry of the Tertiary granitic intrusions in the Eastern Pontides, Turkey. J. Asian Earth Sci. 27, 177–193. https://doi.org/10.1016/j.jseaes.2005.03.002

Asiabanha, A., Foden, J., 2012. Post-collisional transition from an extensional volcano-sedimentary basin to a continental arc in the Alborz Ranges, N-Iran. Lithos 148, 98–111. https://doi.org/10.1016/j.lithos.2012.05.014

Azizi, H., Jahangiri, A., 2008. Cretaceous subduction-related volcanism in the northern Sanandaj-Sirjan Zone, Iran. J. Geodyn. 45, 178–190. https://doi.org/10.1016/j.jog.2007.11.001

Azizi, H., Moinevaziri, H., 2009. Review of the tectonic setting of Cretaceous to Quaternary volcanism in northwestern Iran. J. Geodyn. 47, 167–179. https://doi.org/10.1016/j.jog.2008.12.002

Babazadeh, S., Ghalamghash, J., Furman, T., D'Antonio, M., Raeisi, D., 2021. The Oligocene Avaj volcanic – plutonic complex of Central Iran: A record of magma evolution and mineral equilibria. J. Asian Earth Sci. 222, 104962. https://doi.org/10.1016/j.jseaes.2021.104962

Balcone-Boissard, H., Boudon, G., D'Augustin, T., Erdmann, S., Deloule, E., Vicente, J., 2023. Architecture of the Lesser Antilles Arc Illustrated by Melt Inclusions. J. Petrol. 64. https://doi.org/10.1093/petrology/egad020

Ballato, P., Stockli, D.F., Ghassemi, M.R., Landgraf, A., Strecker, M.R., Hassanzadeh, J., Friedrich, A., Tabatabaei, S.H., 2013. Accommodation of transpressional strain in the Arabia-Eurasia collision zone: new constraints from (U-Th)/He thermochronology in the Alborz mountains, north Iran. Tectonics 32, 1–18. https://doi.org/10.1029/2012TC003159

Ballato, P., Uba, C.E., Landgraf, A., Strecker, M.R., Sudo, M., Stockli, D.F., Friedrich, A., Tabatabaei, S.H., 2011. Arabia-Eurasia continental collision: Insights from late Tertiary foreland-basin evolution in the Alborz Mountains, northern Iran. Geol. Soc. Am. Bull. 123, 106–131. https://doi.org/10.1130/B30091.1

Beerling, D.J., Royer, D.L., 2011. Convergent Cenozoic CO2 history. Nat. Geosci. 4, 418–420. https://doi.org/10.1038/ngeo1186

Berberian, F., Muir, I.D., Pankhurst, R.J., Berberian, M., 1982. Late Cretaceous and early Miocene Andean-type plutonic activity in northern Makran and Central Iran. J. Geol. Soc. London. 139, 605–614. https://doi.org/10.1144/gsjgs.139.5.0605

Berberian, M., 1983. The southern Caspian: a compressional depression floored by a trapped, modified oceanic crust. Can. J. Earth Sci. 20, 163–183.

Berberian, M., King, G.C.P., 1981. Towards a paleogeography and tectonic evolution of Iran: Reply. Can. J. Earth Sci. 18, 1764–1766. https://doi.org/10.1139/e81-163

Berner, R.A., 2003. The long-term carbon cycle, fossil fuels and atmospheric composition. Nature 426, 323–326. https://doi.org/10.1038/nature02131
Berner, R.A., Lasaga, A.C., 1989. Modeling the Geochemical Carbon Cycle. Sci. Am. 260, 74–81. https://doi.org/10.1038/scientificamerican0389-74
Bijl, P.K., Houben, A.J.P., Schouten, S., Bohaty, S.M., Sluijs, A., Reichart, G.-J., Sinninghe Damsté, J.S., Brinkhuis, H., 2010. Transient Middle Eocene Atmospheric CO 2 and Temperature Variations. Science (80-.). 330, 819–821. https://doi.org/10.1126/science.1193654
Bohaty, S.M., Zachos, J.C., Florindo, F., Delaney, M.L., 2009. Coupled greenhouse warming and deep-sea acidification in the middle Eocene. Paleoceanography 24. https://doi.org/10.1029/2008PA001676
Boutoux, A., Briaud, A., Faccenna, C., Ballato, P., Rossetti, F., Blanc, E., 2021. Slab Folding and Surface Deformation of the Iran Mobile Belt. Tectonics 40. https://doi.org/10.1029/2020TC006300
Bucholz, C.E., Gaetani, G.A., Behn, M.D., Shimizu, N., 2013. Post-entrapment modification of volatiles and oxygen fugacity in olivine-hosted melt inclusions. Earth Planet. Sci. Lett. 374, 145–155. https://doi.org/10.1016/j.epsl.2013.05.033
Burton, M., Aiuppa, A., Allard, P., Asensio-Ramos, M., Cofrades, A.P., La Spina, A., Nicholson, E.J., Zanon, V., Barrancos, J., Bitetto, M., Hartley, M., Romero, J.E., Waters, E., Stewart, A., Hernández, P.A., Lages, J.P., Padrón, E., Wood, K., Esse, B., Hayer, C., Cyrzan, K., Rose-Koga, E.F., Schiavi, F., D'Auria, L., Pérez, N.M., 2023. Exceptional eruptive CO2 emissions from intra-plate alkaline magmatism in the Canary volcanic archipelago. Commun. Earth Environ. 4, 467. https://doi.org/10.1038/s43247-023-01103-x
Caricchi, L., Sheldrake, T.E., Blundy, J., 2018. Modulation of magmatic processes by CO2 flushing. Earth Planet. Sci. Lett. 491, 160–171. https://doi.org/10.1016/j.epsl.2018.03.042
Carr, M.J., Gazel, E., 2017. Igpet software for modeling igneous processes: examples of application using the open educational version. Mineral. Petrol. 111, 283–289. https://doi.org/10.1007/s00710-016-0473-z
Castrogiovanni, L., Sternai, P., Piana Agostinetti, N., Pasquero, C., 2024. A reversible-jump Markov chain Monte Carlo algorithm to estimate paleo surface CO2 fluxes linking temperature to atmospheric CO2 concentration time series. Comput. Geosci. 105838. https://doi.org/10.1016/j.cageo.2024.105838
Cloetingh, S., Sternai, P., Koptev, A., Ehlers, T.A., Gerya, T., Kovács, I., Oerlemans, J., Beekman, F., Lavallée, Y., Dingwell, D., Békési, E., Porkolàb, K., Tesauro, M., Lavecchia, A., Botsyun, S., Muller, V., Roure, F., Serpelloni, E., Matenco, L., Castelltort, S., Giovannelli, D., Brovarone, A.V., Malaspina, N., Coletti, G., Valla, P., Limberger, J., 2023. Coupled surface to deep Earth processes: Perspectives from TOPO-EUROPE with an emphasis on climate- and energy-related societal challenges. Glob. Planet. Change 226, 104140. https://doi.org/10.1016/j.gloplacha.2023.104140
Colthup, N.B., Daly, L.H., Wiberly, S.E., 1975. Introduction to infrared and Raman spectroscopy, 2nd editio. ed. Academic Prss, New York.
Costa, F., Morgan, D., 2010. Time Constraints from Chemical Equilibration in Magmatic Crystals, Timescales of Magmatic Processes: From Core to Atmosphere. John Wiley & Sons, Ltd, Chichester, UK. https://doi.org/10.1002/9781444328509.ch7
Costa, F., Shea, T., Ubide, T., 2020. Diffusion chronometry and the timescales of magmatic processes. Nat. Rev. Earth Environ. 1, 201–214. https://doi.org/10.1038/s43017-020-0038-x
Courtillot, V.., Renne, P.R., 2003. On the ages of flood basalt events. Comptes Rendus Geosci. 335, 113–140. https://doi.org/10.1016/S1631-0713(03)00006-3
Cramwinckel, M.J., van der Ploeg, R., Bijl, P.K., Peterse, F., Bohaty, S.M., Röhl, U., Schouten, S., Middelburg, J.J., Sluijs, A., 2019. Harmful algae and export production collapse in the equatorial Atlantic during the zenith of Middle Eocene Climatic Optimum warmth. Geology 47, 247–250. https://doi.org/10.1130/G45614.1
Deegan, F.M., Troll, V.R., Freda, C., Misiti, V., Chadwick, J.P., McLeod, C.L., Davidson, J.P., 2010. Magma–Carbonate Interaction Processes and Associated CO2 Release at Merapi Volcano, Indonesia: Insights from Experimental Petrology. J. Petrol. 51, 1027–1051. https://doi.org/10.1093/petrology/egq010
Dewey, J.F., Pitman, W.C., Ryan, W.B.F., Bonnin, J., 1973. Plate Tectonics and the Evolution of the Alpine System. Geol. Soc. Am. Bull. 84, 3137. https://doi.org/10.1130/0016-7606(1973)84<3137:PTATEO>2.0.CO;2
Donnadieu, Y., Pierrehumbert, R., Jacob, R., Fluteau, F., 2006. Modelling the primary control of paleogeography on Cretaceous climate. Earth Planet. Sci. Lett. 248, 426–437. https://doi.org/10.1016/j.epsl.2006.06.007
Ducea, M., 2001. The California Arc: Thick Granitic Batholiths, Eclogitic Residues, Lithospheric-Scale Thrusting, and Magmatic Flare-Ups. GSA Today 11, 4. https://doi.org/10.1130/1052-5173(2001)011<0004:TCATGB>2.0.CO;2
Ducea, M.N., Barton, M.D., 2007. Igniting flare-up events in Cordilleran arcs. Geology 35, 1047. https://doi.org/10.1130/G23898A.1

Ebadi, S., Barzaghi, R., Safari, A., Bahroudi, A., 2019. Evaluation of different gravimetric methods to Moho recovery in Iran. Ann. Geophys. 62. https://doi.org/10.4401/ag-8054

Edgar, K.M., Bohaty, S.M., Gibbs, S.J., Sexton, P.F., Norris, R.D., Wilson, P.A., 2013. Symbiont "bleaching" in planktic foraminifera during the Middle Eocene Climatic Optimum. Geology 41, 15–18. https://doi.org/10.1130/G33388.1

Esposito, R., 2021. Chapter 7: A protocol and review methods to select, analyze and interpret melt inclusions to determine pre-eruptive volatile contents of magmas, in: Fluid and Melt Inclusions: Applications to Geologic Processes. MAC, pp. 1–32.

Esposito, R., Bodnar, R.J., Danyushevsky, L. V., De Vivo, B., Fedele, L., Hunter, J., Lima, A., Shimizu, N., 2011. Volatile Evolution of Magma Associated with the Solchiaro Eruption in the Phlegrean Volcanic District (Italy). J. Petrol. 52, 2431–2460. https://doi.org/10.1093/petrology/egr051

Esposito, R., Klebesz, R., Bartoli, O., Klyukin, Y., Moncada, D., Doherty, A., Bodnar, R., 2012. Application of the Linkam TS1400XY heating stage to melt inclusion studies. Open Geosci. 4, 208–218. https://doi.org/10.2478/s13533-011-0054-y

Esposito, R., Lamadrid, H.M., Redi, D., Steele-MacInnis, M., Bodnar, R.J., Manning, C.E., De Vivo, B., Cannatelli, C., Lima, A., 2016. Detection of liquid H 2 O in vapor bubbles in reheated melt inclusions: Implications for magmatic fluid composition and volatile budgets of magmas? Am. Mineral. 101, 1691–1695. https://doi.org/10.2138/am-2016-5689

Esposito, R., Redi, D., Danyushevsky, L. V., Gurenko, A., De Vivo, B., Manning, C.E., Bodnar, R.J., Steele-MacInnis, M., Frezzotti, M.-L., 2023. Constraining the volatile evolution of mafic melts at Mt. Somma–Vesuvius, Italy, based on the composition of reheated melt inclusions and their olivine hosts. Eur. J. Mineral. 35, 921–948. https://doi.org/10.5194/ejm-35-921-2023

Fakhari, M.D., Axen, G.J., Horton, B.K., Hassanzadeh, J., Amini, A., 2008. Revised age of proximal deposits in the Zagros foreland basin and implications for Cenozoic evolution of the High Zagros. Tectonophysics 451, 170–185. https://doi.org/10.1016/j.tecto.2007.11.064

Falcon, N.L., 1974. Southern Iran: Zagros Mountains, in: Spencer, A.M. (Ed.), Mesozoic-Cenozoic Orogenic Belts, Data for Orogenic Studies: Alpine-Himalayan Orogens. Geological Society, London, Special Publications, pp. 199–211.

Förster, H., Fesefeldt, K., Kürsten, M., 1972. Magmatic and orogenic evolution of the central Iranian volcanic belt, in: Armstrong, J.E., Hedberg, H.D. (Eds.), 24th International Geologic Congress. Int. Geol. Congr., Montreal, QC, Canada, pp. 198–210.

Foster, G.L., Royer, D.L., Lunt, D.J., 2017. Future climate forcing potentially without precedent in the last 420 million years. Nat. Commun. 8, 14845. https://doi.org/10.1038/ncomms14845

Freundt, A., Grevemeyer, I., Rabbel, W., Hansteen, T.H., Hensen, C., Wehrmann, H., Kutterolf, S., Halama, R., Frische, M., 2014. Volatile (H2O, CO2, Cl, S) budget of the Central American subduction zone. Int. J. Earth Sci. 103, 2101–2127. https://doi.org/10.1007/s00531-014-1001-1

Frezzotti, M.L., Tecce, F., Casagli, A., 2012. Raman spectroscopy for fluid inclusion analysis. J. Geochemical Explor. 112, 1–20. https://doi.org/10.1016/j.gexplo.2011.09.009

Gaetani, G.A., O'Leary, J.A., Shimizu, N., Bucholz, C.E., Newville, M., 2012. Rapid reequilibration of H2O and oxygen fugacity in olivine-hosted melt inclusions. Geology 40, 915–918. https://doi.org/10.1130/G32992.1

Ganino, C., Arndt, N.T., 2009. Climate changes caused by degassing of sediments during the emplacement of large igneous provinces. Geology 37, 323–326. https://doi.org/10.1130/G25325A.1

Gans, P.B., Mahood, G. A., Schermer, E., 1989. Synextensional magmatism in the Basin and Range Province; A case study from the eastern Great Basin, Geological Society of America Special Papers. Geological Society of America. https://doi.org/10.1130/SPE233

Garrabos, Y., Tufev, R., Le Neindre, B., Zalczer, G., Beysens, D., 1980. Rayleigh and Raman scattering near the critical point of carbon dioxide. J. Chem. Phys. 72, 4637–4651.

Geological Survey and Mineral Exploration of Iran, 2006. Khoja geological map (Iran).

Geological Survey and Mineral Exploration of Iran, 1995. Karaj geological map (Iran) - series n. 6161.

Ghiorso, M.S., Gualda, G.A.R., 2015. An H2O–CO2 mixed fluid saturation model compatible with rhyolite-MELTS. Contrib. to Mineral. Petrol. 169, 53. https://doi.org/10.1007/s00410-015-1141-8

Golonka, J., 2004. Plate tectonic evolution of the southern margin of Eurasia in the Mesozoic and Cenozoic. Tectonophysics 381, 235–273. https://doi.org/10.1016/j.tecto.2002.06.004

Gualda, G.A.R., Ghiorso, M.S., Lemons, R. V., Carley, T.L., 2012. Rhyolite-MELTS: a Modified Calibration of MELTS Optimized for Silica-rich, Fluid-bearing Magmatic Systems. J. Petrol. 53, 875–890. https://doi.org/10.1093/petrology/egr080

Hansen, J., Sato, M., Russell, G., Kharecha, P., 2013. Climate sensitivity, sea level and atmospheric carbon dioxide. Philos. Trans. R. Soc. A Math. Phys. Eng. Sci. 371, 20120294. https://doi.org/10.1098/rsta.2012.0294

Hartley, M.E., Maclennan, J., Edmonds, M., Thordarson, T., 2014. Reconstructing the deep CO2 degassing behaviour of large basaltic fissure eruptions. Earth Planet. Sci. Lett. 393, 120–131. https://doi.org/10.1016/j.epsl.2014.02.031

Hatzfeld, D., Molnar, P., 2010. Comparisons of the kinematics and deep structures of the Zagros and Himalaya and of the Iranian and Tibetan plateaus and geodynamic implications. Rev. Geophys. 48, RG2005. https://doi.org/10.1029/2009RG000304

Hauri, E., 2002. SIMS analysis of volatiles in silicate glasses, 2: isotopes and abundances in Hawaiian melt inclusions. Chem. Geol. 183, 115–141. https://doi.org/10.1016/S0009-2541(01)00374-6

Henehan, M.J., Edgar, K.M., Foster, G.L., Penman, D.E., Hull, P.M., Greenop, R., Anagnostou, E., Pearson, P.N., 2020. Revisiting the Middle Eocene Climatic Optimum "Carbon Cycle Conundrum" With New Estimates of Atmospheric pCO 2 From Boron Isotopes. Paleoceanogr. Paleoclimatology 35. https://doi.org/10.1029/2019PA003713

Hoareau, G., Bomou, B., van Hinsbergen, D.J.J., Carry, N., Marquer, D., Donnadieu, Y., Le Hir, G., Vrielynck, B., Walter-Simonnet, A.-V., 2015. Did high Neo-Tethys subduction rates contribute to early Cenozoic warming? Clim. Past 11, 1751–1767. https://doi.org/10.5194/cp-11-1751-2015

Iacono-Marziano, G., Gaillard, F., Scaillet, B., Pichavant, M., Chiodini, G., 2009. Role of non-mantle CO2 in the dynamics of volcano degassing: The Mount Vesuvius example. Geology 37, 319–322. https://doi.org/10.1130/G25446A.1

Jolivet, L., Faccenna, C., 2000. Mediterranean extension and the Africa-Eurasia collision. Tectonics 19, 1095–1106. https://doi.org/10.1029/2000TC900018

Judd, E.J., Tierney, J.E., Lunt, D.J., Montañez, I.P.P., Huber, B.T., Wing, S.L., Valdes, P.J., 2024. A 485-million-year history of Earth's surface temperature. Science (80-.). 385. https://doi.org/10.1126/science.adk3705

Kazmin, V.G., Sbortshikov, I.M., Ricou, L.-E., Zonenshain, L.P., Boulin, J., Knipper, A.L., 1986. Volcanic belts as markers of the Mesozoic-Cenozoic active margin of Eurasia. Tectonophysics 123, 123–152. https://doi.org/10.1016/0040-1951(86)90195-2

Klébesz, R., Esposito, R., De Vivo, B., Bodnar, R.J., 2015. Constraints on the origin of sub-effusive nodules from the Sarno (Pomici di Base) eruption of Mt. Somma-Vesuvius (Italy) based on compositions of silicate-melt inclusions and clinopyroxene. Am. Mineral. 100, 760–773. https://doi.org/10.2138/am-2015-4958

Koshnaw, R.I., Stockli, D.F., Schlunegger, F., 2019. Timing of the Arabia-Eurasia continental collision—Evidence from detrital zircon U-Pb geochronology of the Red Bed Series strata of the northwest Zagros hinterland, Kurdistan region of Iraq. Geology 47, 47–50. https://doi.org/10.1130/G45499.1

Le Bas, M.J.L., Maitre, R.W.L., Streckeisen, A., Zanettin, B., 1986. A Chemical Classification of Volcanic Rocks Based on the Total Alkali-Silica Diagram. J. Petrol. 27, 745–750. https://doi.org/10.1093/petrology/27.3.745

Lee, C.-T.A., Lackey, J.S., 2015. Global Continental Arc Flare-ups and Their Relation to Long-Term Greenhouse Conditions. Elements 11, 125–130. https://doi.org/10.2113/gselements.11.2.125

Lee, C.-T.A., Shen, B., Slotnick, B.S., Liao, K., Dickens, G.R., Yokoyama, Y., Lenardic, A., Dasgupta, R., Jellinek, M., Lackey, J.S., Schneider, T., Tice, M.M., 2013. Continental arc-island arc fluctuations, growth of crustal carbonates, and long-term climate change. Geosphere 9, 21–36. https://doi.org/10.1130/GES00822.1

Lefebvre, V., Donnadieu, Y., Goddéris, Y., Fluteau, F., Hubert-Théou, L., 2013. Was the Antarctic glaciation delayed by a high degassing rate during the early Cenozoic? Earth Planet. Sci. Lett. 371–372, 203–211. https://doi.org/10.1016/j.epsl.2013.03.049

Lowenstern, J.B., 2003. Melt inclusions come of age: Volatiles, volcanoes, and sorby's legacy. pp. 1–21. https://doi.org/10.1016/S1871-644X(03)80021-9

Lowenstern, J.B., 1995. Applications of silicate-melt inclusions to the study of magmatic volatiles., in: Thompson, J.F.H. (Ed.), Magmas, Fluids and Ore Deposition. Mineral. Assoc. Canada, pp. 71–99.

Ma, Y., Fan, M., Zhang, C., Grasby, S.E., Yin, R., Lu, Yangbo, Zhang, B., Jin, X., Ma, C., Lu, Yongchao, Sluijs, A., 2024. Volcanic and orbitally forced carbon release during the Middle Eocene Climatic Optimum. Geology 52, 813–818. https://doi.org/10.1130/G52435.1

Macdonald, R., Belkin, H.E., Fitton, J.G., Rogers, N.W., Nejbert, K., Tindle, A.G., Marshall, A.S., 2008. The Roles of Fractional Crystallization, Magma Mixing, Crystal Mush Remobilization and Volatile–Melt Interactions in the Genesis of a Young Basalt–Peralkaline Rhyolite Suite, the Greater Olkaria Volcanic Complex, Kenya Rift Valley. J. Petrol. 49, 1515–1547. https://doi.org/10.1093/petrology/egn036

Madanipour, S., Yassaghi, A., Ehlers, T.A., Enkelmann, E., 2018. Tectonostratigraphy, structural geometry and kinematics of the NW Iranian Plateau margin: Insights from the Talesh Mountains, Iran. Am. J. Sci. 318, 208–245. https://doi.org/10.2475/02.2018.02

Marty, B., Tolstikhin, I.N., 1998. CO2 fluxes from mid-ocean ridges, arcs and plumes. Chem. Geol. 145, 233–

248. https://doi.org/10.1016/S0009-2541(97)00145-9
Masotta, M., Mollo, S., Freda, C., Gaeta, M., Moore, G., 2013. Clinopyroxene–liquid thermometers and barometers specific to alkaline differentiated magmas. Contrib. to Mineral. Petrol. 166, 1545–1561. https://doi.org/10.1007/s00410-013-0927-9
McKenzie, N.R., Horton, B.K., Loomis, S.E., Stockli, D.F., Planavsky, N.J., Lee, C.-T.A., 2016. Continental arc volcanism as the principal driver of icehouse-greenhouse variability. Science (80-.). 352, 444–447. https://doi.org/10.1126/science.aad5787
McQuarrie, N., Stock, J.M., Verdel, C., Wernicke, B.P., 2003. Cenozoic evolution of Neotethys and implications for the causes of plate motions. Geophys. Res. Lett. 30. https://doi.org/10.1029/2003GL017992
McQuarrie, N., van Hinsbergen, D.J.J., 2013. Retrodeforming the Arabia-Eurasia collision zone: Age of collision versus magnitude of continental subduction. Geology 41, 315–318. https://doi.org/10.1130/G33591.1
Metrich, N., Wallace, P.J., 2008. Volatile Abundances in Basaltic Magmas and Their Degassing Paths Tracked by Melt Inclusions. Rev. Mineral. Geochemistry 69, 363–402. https://doi.org/10.2138/rmg.2008.69.10
Moore, L.R., Gazel, E., Tuohy, R., Lloyd, A.S., Esposito, R., Steele-MacInnis, M., Hauri, E.H., Wallace, P.J., Plank, T., Bodnar, R.J., 2015. Bubbles matter: An assessment of the contribution of vapor bubbles to melt inclusion volatile budgets. Am. Mineral. 100, 806–823. https://doi.org/10.2138/am-2015-5036
Morley, C.K., Kongwung, B., Julapour, A.A., Abdolghafourian, M., Hajian, M., Waples, D., Warren, J., Otterdoom, H., Srisuriyon, K., Kazemi, H., 2009. Structural development of a major late Cenozoic basin and transpressional belt in central Iran: The Central Basin in the Qom-Saveh area. Geosphere 5, 325–362. https://doi.org/10.1130/GES00223.1
Nalivkin, D., 1976. Geological Map of Caucasus, Scale 1: 500,000.
Narváez, D.F., Samaniego, P., Koga, K.T., Rose-Koga, E.F., Hidalgo, S., Ratzov, G., 2023. Two types of slab components under Ecuadorian volcanoes supported by primitive olivine-hosted melt inclusion study. Lithos 442–443, 107049. https://doi.org/10.1016/j.lithos.2023.107049
Newman, S., Lowenstern, J.B., 2002. VolatileCalc: a silicate melt–H2O–CO2 solution model written in Visual Basic for excel. Comput. Geosci. 28, 597–604. https://doi.org/10.1016/S0098-3004(01)00081-4
Pearce, J.A., Bender, J.F., De Long, S.E., Kidd, W.S.F., Low, P.J., Güner, Y., Saroglu, F., Yilmaz, Y., Moorbath, S., Mitchell, J.G., 1990. Genesis of collision volcanism in Eastern Anatolia, Turkey. J. Volcanol. Geotherm. Res. 44, 189–229. https://doi.org/10.1016/0377-0273(90)90018-B
Petrone, C.M., Bugatti, G., Braschi, E., Tommasini, S., 2016. Pre-eruptive magmatic processes re-timed using a non-isothermal approach to magma chamber dynamics. Nat. Commun. 7, 12946. https://doi.org/10.1038/ncomms12946
Pirouz, M., Avouac, J.-P., Hassanzadeh, J., Kirschvink, J.L., Bahroudi, A., 2017. Early Neogene foreland of the Zagros, implications for the initial closure of the Neo-Tethys and kinematics of crustal shortening. Earth Planet. Sci. Lett. 477, 168–182. https://doi.org/10.1016/j.epsl.2017.07.046
Portnyagin, M., Almeev, R., Matveev, S., Holtz, F., 2008. Experimental evidence for rapid water exchange between melt inclusions in olivine and host magma. Earth Planet. Sci. Lett. 272, 541–552. https://doi.org/10.1016/j.epsl.2008.05.020
Putirka, K.D., 2008. Thermometers and Barometers for Volcanic Systems. Rev. Mineral. Geochemistry 69, 61–120. https://doi.org/10.2138/rmg.2008.69.3
Rabiee, A., Rossetti, F., Asahara, Y., Azizi, H., Lucci, F., Lustrino, M., Nozaem, R., 2020. Long-lived, Eocene-Miocene stationary magmatism in NW Iran along a transform plate boundary. Gondwana Res. 85, 237–262. https://doi.org/10.1016/j.gr.2020.03.014
Raymo, M.E., Ruddiman, W.F., 1992. Tectonic forcing of late Cenozoic climate. Nature 359, 117–122. https://doi.org/10.1038/359117a0
Remigi, S., Mancini, T., Ferrando, S., Frezzotti, M.L., 2021. Interlaboratory Application of Raman CO 2 Densimeter Equations: Experimental Procedure and Statistical Analysis Using Bootstrapped Confidence Intervals. Appl. Spectrosc. 75, 867–881. https://doi.org/10.1177/0003702820987601
Roedder, E., 1979. Origin and significance of magmatic inclusions. Bull. Minéralogie 102, 487–510.
Rose-Koga, E.F., Bouvier, A.-S., Gaetani, G.A., Wallace, P.J., Allison, C.M., Andrys, J.A., Angeles de la Torre, C.A., Barth, A., Bodnar, R.J., Bracco Gartner, A.J.J., Butters, D., Castillejo, A., Chilson-Parks, B., Choudhary, B.R., Cluzel, N., Cole, M., Cottrell, E., Daly, A., Danyushevsky, L.V., DeVitre, C.L., Drignon, M.J., France, L., Gaborieau, M., Garcia, M.O., Gatti, E., Genske, F.S., Hartley, M.E., Hughes, E.C., Iveson, A.A., Johnson, E.R., Jones, M., Kagoshima, T., Katzir, Y., Kawaguchi, M., Kawamoto, T., Kelley, K.A., Koornneef, J.M., Kurz, M.D., Laubier, M., Layne, G.D., Lerner, A., Lin, K.-Y., Liu, P.-P., Lorenzo-Merino, A., Luciani, N., Magalhães, N., Marschall, H.R., Michael, P.J., Monteleone, B.D., Moore, L.R., Moussallam, Y., Muth, M., Myers, M.L., Narváez, D.F., Navon, O., Newcombe, M.E., Nichols, A.R.L., Nielsen, R.L., Pamukcu, A., Plank, T., Rasmussen, D.J., Roberge, J., Schiavi, F.,

Schwartz, D., Shimizu, K., Shimizu, K., Shimizu, N., Thomas, J.B., Thompson, G.T., Tucker, J.M., Ustunisik, G., Waelkens, C., Zhang, Y., Zhou, T., 2021. Silicate melt inclusions in the new millennium: A review of recommended practices for preparation, analysis, and data presentation. Chem. Geol. 570, 120145. https://doi.org/10.1016/j.chemgeo.2021.120145

Rose-Koga, E.F., Koga, K.T., Hamada, M., Hélouis, T., Whitehouse, M.J., Shimizu, N., 2014. Volatile (F and Cl) concentrations in Iwate olivine-hosted melt inclusions indicating low-temperature subduction. Earth, Planets Sp. 66, 81. https://doi.org/10.1186/1880-5981-66-81

Sahandi, R., Soheili, M., Sadeghi, M., Delavar, T., Jafari Rad, A., 2014. Compiled geological map of Iran, scale 1 : 1 000 000.

Salehi, N., Torkian, A., Furman, T., 2020. Olivine-hosted melt inclusions in Pliocene–Quaternary lavas from the Qorveh–Bijar volcanic belt, western Iran: implications for source lithology and cooling history. Int. Geol. Rev. 62, 1828–1844. https://doi.org/10.1080/00206814.2018.1564890

Self, S., Widdowson, M., Thordarson, T., Jay, A.E., 2006. Volatile fluxes during flood basalt eruptions and potential effects on the global environment: A Deccan perspective. Earth Planet. Sci. Lett. 248, 518–532. https://doi.org/10.1016/j.epsl.2006.05.041

Seton, M., Müller, R.D., Zahirovic, S., Gaina, C., Torsvik, T., Shephard, G., Talsma, A., Gurnis, M., Turner, M., Maus, S., Chandler, M., 2012. Global continental and ocean basin reconstructions since 200Ma. Earth-Science Rev. 113, 212–270. https://doi.org/10.1016/j.earscirev.2012.03.002

Shafaii Moghadam, H., Li, X.-H., Ling, X.X., Santos, J.F., Stern, R.J., Li, Q.-L., Ghorbani, G., 2015. Eocene Kashmar granitoids (NE Iran): Petrogenetic constraints from U–Pb zircon geochronology and isotope geochemistry. Lithos 216–217, 118–135. https://doi.org/10.1016/j.lithos.2014.12.012

Simon, J.I., Renne, P.R., Mundil, R., 2008. Implications of pre-eruptive magmatic histories of zircons for U–Pb geochronology of silicic extrusions. Earth Planet. Sci. Lett. 266, 182–194. https://doi.org/10.1016/j.epsl.2007.11.014

Sluijs, A., Zeebe, R.E., Bijl, P.K., Bohaty, S.M., 2013. A middle Eocene carbon cycle conundrum. Nat. Geosci. 6, 429–434. https://doi.org/10.1038/ngeo1807

Sobolev, A.V., 1996. Melt inclusions in minerals as a source of principle petrological information. Petrology 4, 228–239.

Sobolev, A. V., Danyushevsky, L. V., 1994. Petrology and Geochemistry of Boninites from the North Termination of the Tonga Trench: Constraints on the Generation Conditions of Primary High-Ca Boninite Magmas. J. Petrol. 35, 1183–1211. https://doi.org/10.1093/petrology/35.5.1183

Steele-Macinnis, M., Esposito, R., Bodnar, R.J., 2011. Thermodynamic Model for the Effect of Post-entrapment Crystallization on the H2O-CO2 Systematics of Vapor-saturated, Silicate Melt Inclusions. J. Petrol. 52, 2461–2482. https://doi.org/10.1093/petrology/egr052

Sternai, P., 2023. Feedbacks Between Internal and External Earth Dynamics, in: Dynamics of Plate Tectonics and Mantle Convection. Elsevier, pp. 271–294. https://doi.org/10.1016/B978-0-323-85733-8.00019-6

Sternai, P., Caricchi, L., Pasquero, C., Garzanti, E., Hinsbergen, D.J.J., Castelltort, S., 2019. Magmatic Forcing of Cenozoic Climate? J. Geophys. Res. Solid Earth 125. https://doi.org/10.1029/2018JB016460

Stöcklin, J., 1974. Northern Iran: Alborz Mountains. Geol. Soc. London, Spec. Publ. 4, 213–234. https://doi.org/10.1144/GSL.SP.2005.004.01.12

Stöcklin, J., 1968. Structural history and tectonics of Iran: a review. Am. Assoc. Pet. Geol. 52, 1229–1258.

Sundquist, E.T., 2013. Geological Perspectives on Carbon Dioxide and the Carbon Cycle. pp. 55–59. https://doi.org/10.1029/GM032p0005

Tobin, T.S., Bitz, C.M., Archer, D., 2017. Modeling climatic effects of carbon dioxide emissions from Deccan Traps volcanic eruptions around the Cretaceous–Paleogene boundary. Palaeogeogr. Palaeoclimatol. Palaeoecol. 478, 139–148. https://doi.org/10.1016/j.palaeo.2016.05.028

Tucker, J.M., Hauri, E.H., Pietruszka, A.J., Garcia, M.O., Marske, J.P., Trusdell, F.A., 2019. A high carbon content of the Hawaiian mantle from olivine-hosted melt inclusions. Geochim. Cosmochim. Acta 254, 156–172. https://doi.org/10.1016/j.gca.2019.04.001

van der Boon, A., Kuiper, K.F., van der Ploeg, R., Cramwinckel, M.J., Honarmand, M., Sluijs, A., Krijgsman, W., 2021. Exploring a link between the Middle Eocene Climatic Optimum and Neotethys continental arc flare-up. Clim. Past 17, 229–239. https://doi.org/10.5194/cp-17-229-2021

van der Boon, A., Kuiper, K.F., Villa, G., Renema, W., Meijers, M.J.M., Langereis, C.G., Aliyeva, E., Krijgsman, W., 2017. Onset of Maikop sedimentation and cessation of Eocene arc volcanism in the Talysh Mountains, Azerbaijan. Geol. Soc. London, Spec. Publ. 428, 145–169. https://doi.org/10.1144/SP428.3

van der Ploeg, R., Selby, D., Cramwinckel, M.J., Li, Y., Bohaty, S.M., Middelburg, J.J., Sluijs, A., 2018. Middle Eocene greenhouse warming facilitated by diminished weathering feedback. Nat. Commun. 9, 2877. https://doi.org/10.1038/s41467-018-05104-9

Verdel, C., Wernicke, B.P., Hassanzadeh, J., Guest, B., 2011. A Paleogene extensional arc flare-up in Iran.

Tectonics 30, n/a-n/a. https://doi.org/10.1029/2010TC002809
Vernant, P., Nilforoushan, F., Hatzfeld, D., Abbassi, M.R., Vigny, C., Masson, F., Nankali, H., Martinod, J., Ashtiani, A., Bayer, R., Tavakoli, F., Chéry, J., 2004. Present-day crustal deformation and plate kinematics in the Middle East constrained by GPS measurements in Iran and northern Oman. Geophys. J. Int. 157, 381–398. https://doi.org/10.1111/j.1365-246X.2004.02222.x
Vincent, S.J., Allen, M.B., Ismail-Zadeh, A.D., Flecker, R., Foland, K.A., Simmons, M.D.M.D., 2005. Insights from the Talysh of Azerbaijan into the Paleogene evolution of the South Caspian region. Geol. Soc. Am. Bull. 117, 1513. https://doi.org/10.1130/B25690.1
Walker, J.C.G., Hays, P.B., Kasting, J.F., 1981. A negative feedback mechanism for the long-term stabilization of Earth's surface temperature. J. Geophys. Res. 86, 9776. https://doi.org/10.1029/JC086iC10p09776
Wallace, P.J., Anderson, A.T., Davis, A.M., 1999. Gradients in H 2 O, CO 2 , and exsolved gas in a large-volume silicic magma system: Interpreting the record preserved in melt inclusions from the Bishop Tuff. J. Geophys. Res. Solid Earth 104, 20097–20122. https://doi.org/10.1029/1999JB900207
Wallace, P.J., Plank, T., Bodnar, R.J., Gaetani, G.A., Shea, T., 2021. Olivine-Hosted Melt Inclusions: A Microscopic Perspective on a Complex Magmatic World. Annu. Rev. Earth Planet. Sci. 49, 465–494. https://doi.org/10.1146/annurev-earth-082420-060506
Wignall, P.B., Sun, Y., Bond, D.P.G., Izon, G., Newton, R.J., Védrine, S., Widdowson, M., Ali, J.R., Lai, X., Jiang, H., Cope, H., Bottrell, S.H., 2009. Volcanism, Mass Extinction, and Carbon Isotope Fluctuations in the Middle Permian of China. Science (80-.). 324, 1179–1182. https://doi.org/10.1126/science.1171956
Witkowski, J., Bohaty, S.M., McCartney, K., Harwood, D.M., 2012. Enhanced siliceous plankton productivity in response to middle Eocene warming at Southern Ocean ODP Sites 748 and 749. Palaeogeogr. Palaeoclimatol. Palaeoecol. 326–328, 78–94. https://doi.org/10.1016/j.palaeo.2012.02.006
Wojdyr, M., 2010. Fityk : a general-purpose peak fitting program. J. Appl. Crystallogr. 43, 1126–1128. https://doi.org/10.1107/S0021889810030499
Wong, K., Mason, E., Brune, S., East, M., Edmonds, M., Zahirovic, S., 2019. Deep Carbon Cycling Over the Past 200 Million Years: A Review of Fluxes in Different Tectonic Settings. Front. Earth Sci. 7. https://doi.org/10.3389/feart.2019.00263
Yuan, X., Mayanovic, R.A., 2017. An Empirical Study on Raman Peak Fitting and Its Application to Raman Quantitative Research. Appl. Spectrosc. 71, 2325–2338. https://doi.org/10.1177/0003702817721527
Zachos, J., Pagani, M., Sloan, L., Thomas, E., Billups, K., 2001. Trends, Rhythms, and Aberrations in Global Climate 65 Ma to Present. Science (80-.). 292, 686–693. https://doi.org/10.1126/science.1059412
Zhang, S.-H., Ji, W.-Q., Chen, H.-B., Kirstein, L.A., Wu, F.-Y., 2023. Linking rapid eruption of the Linzizong volcanic rocks and Early Eocene Climatic Optimum (EECO): Constraints from the Pana Formation in the Linzhou and Pangduo basins, southern Tibet. Lithos 446–447, 107159. https://doi.org/10.1016/j.lithos.2023.107159

Figures

1232

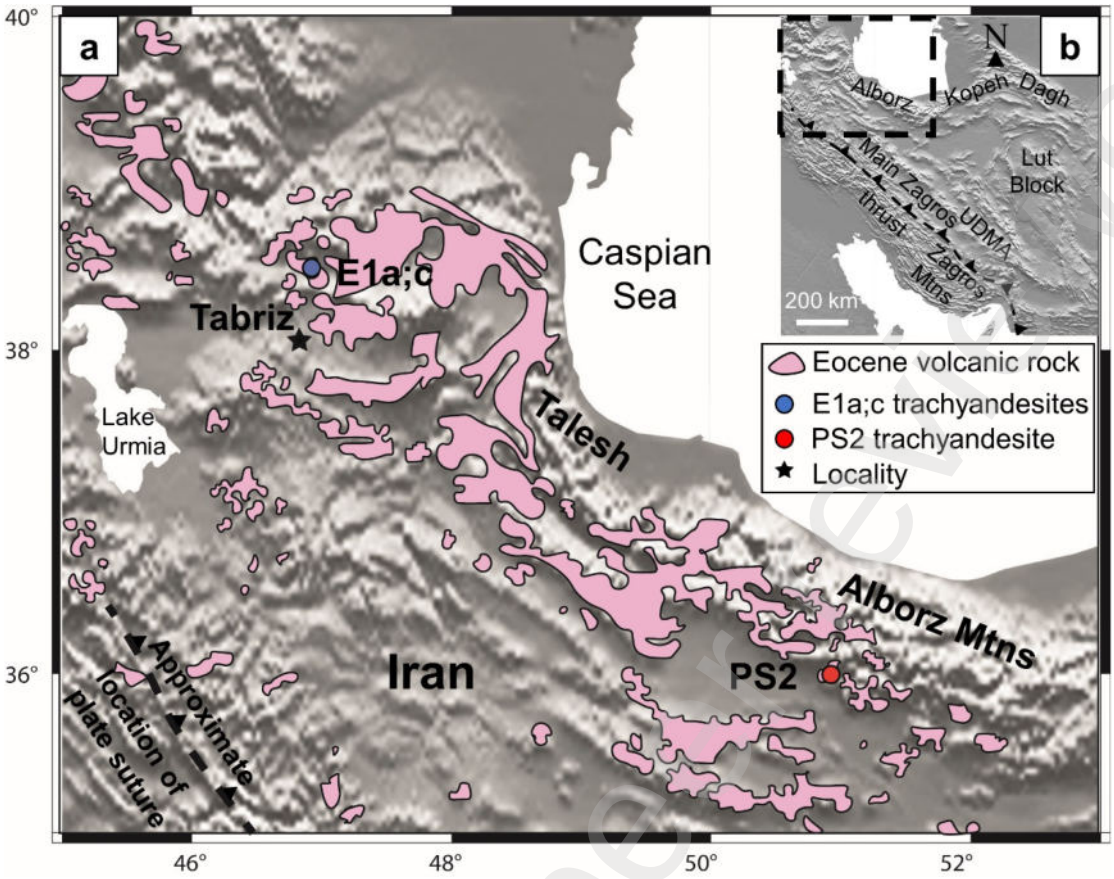

1233

1234 **Figure 1**

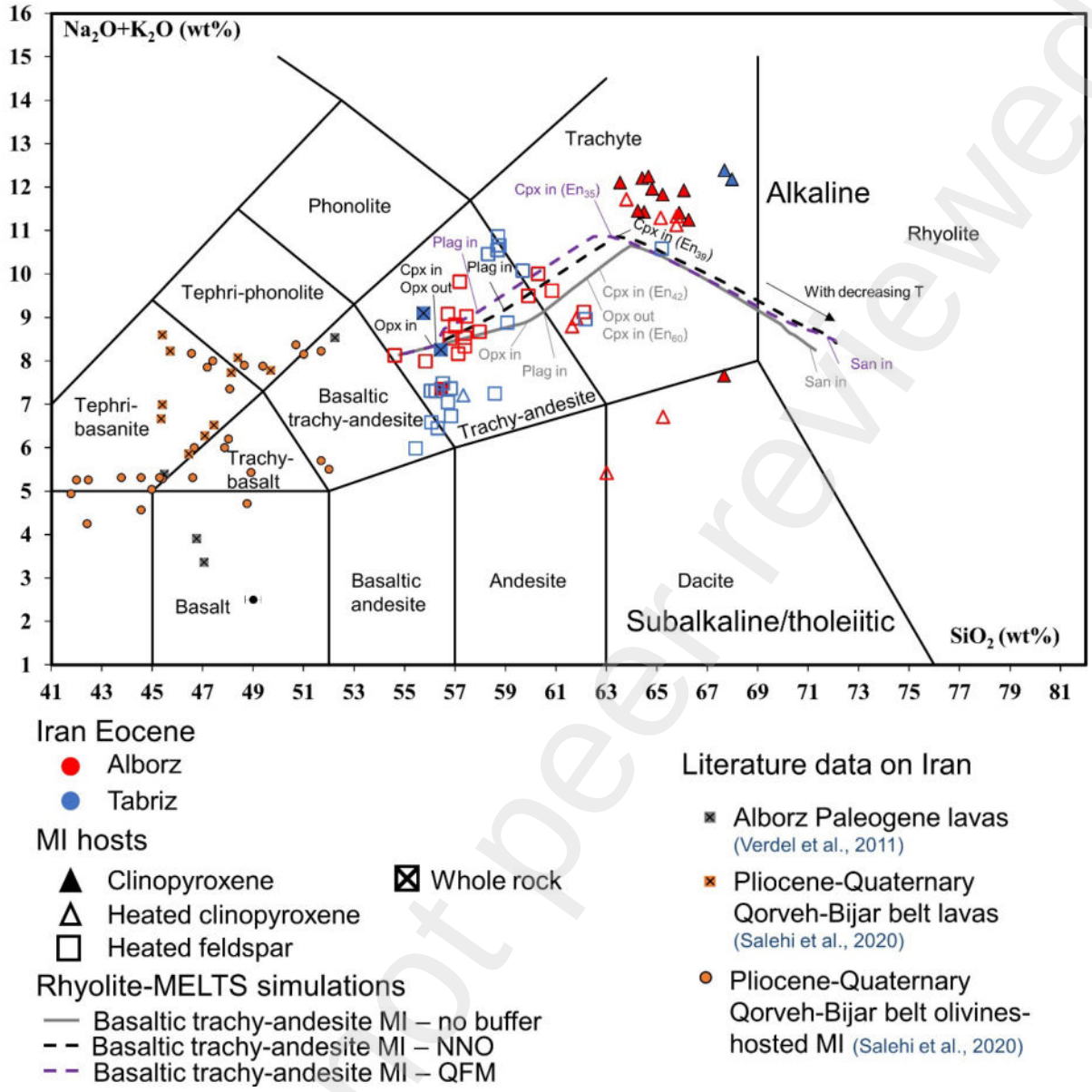

Figure 2

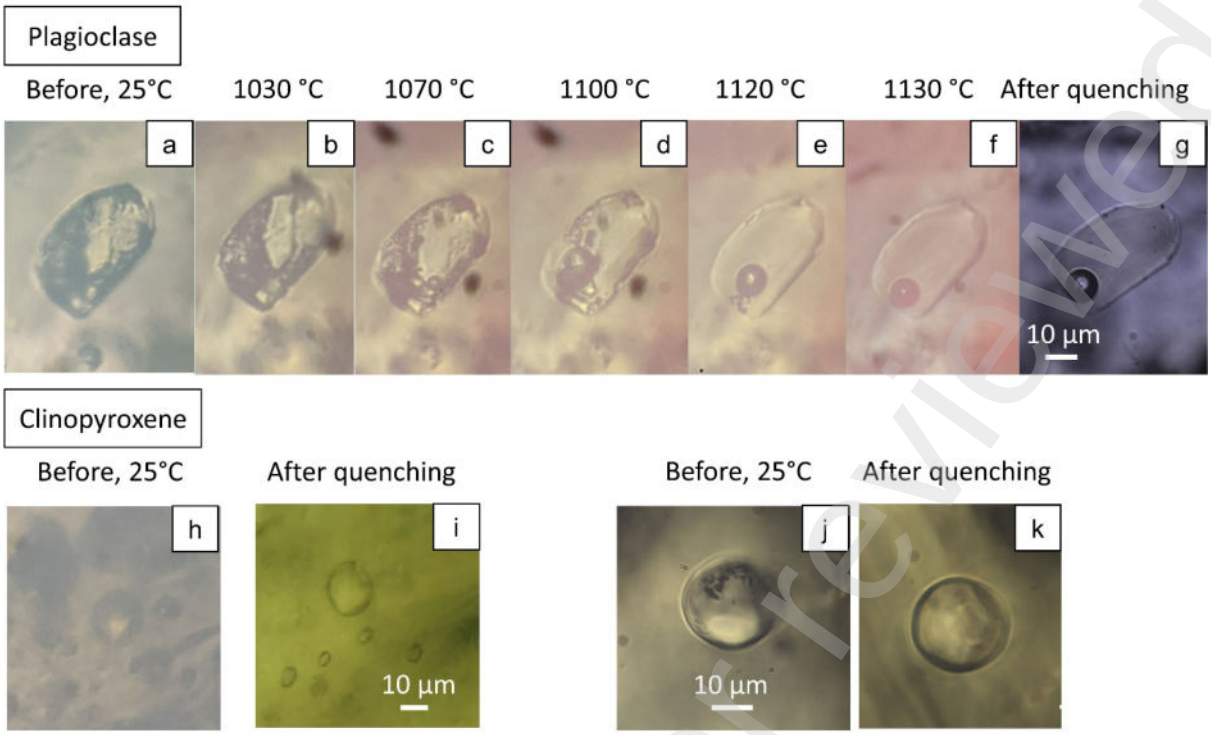

Figure 3

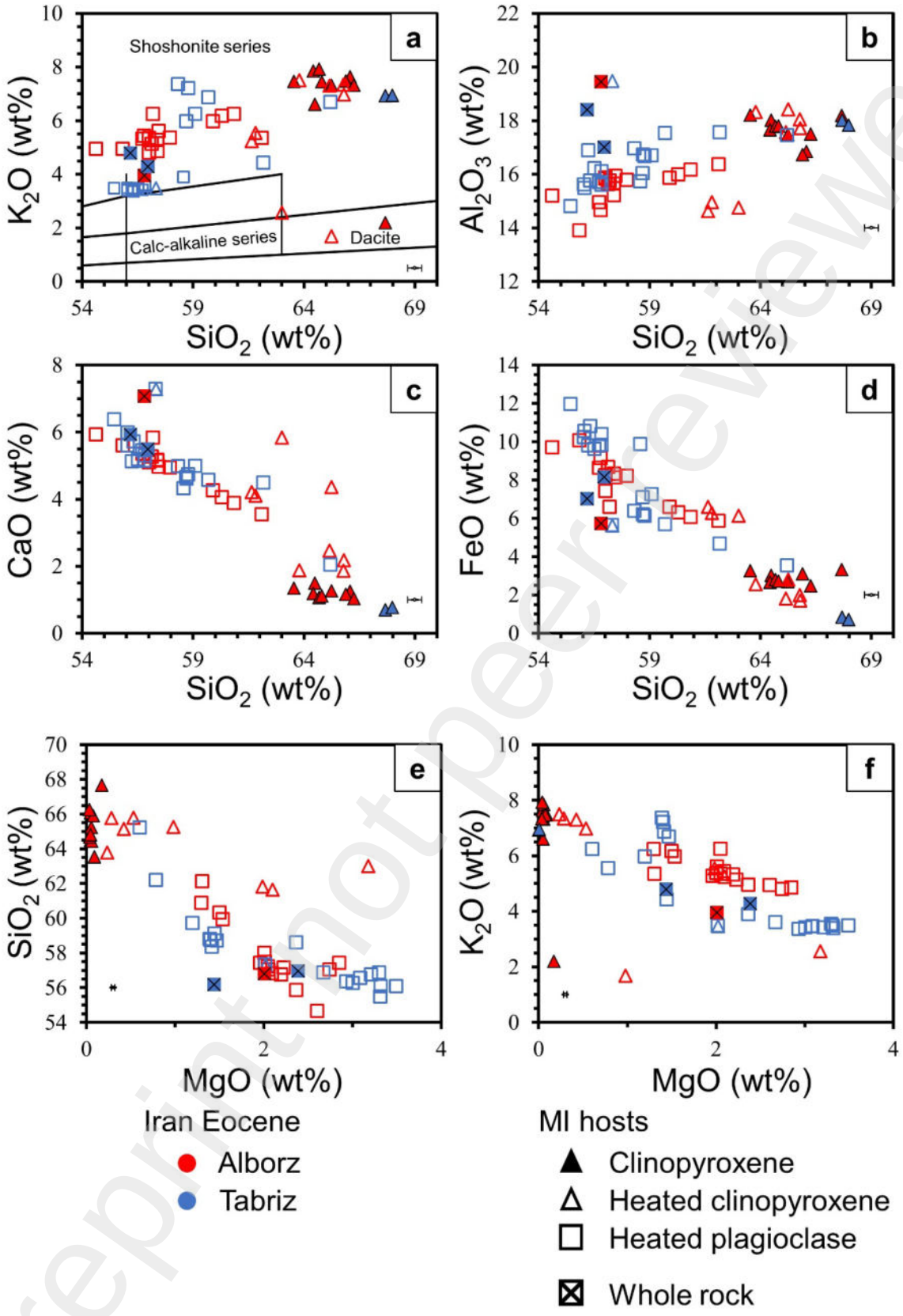

1241

1242 **Figure 4**

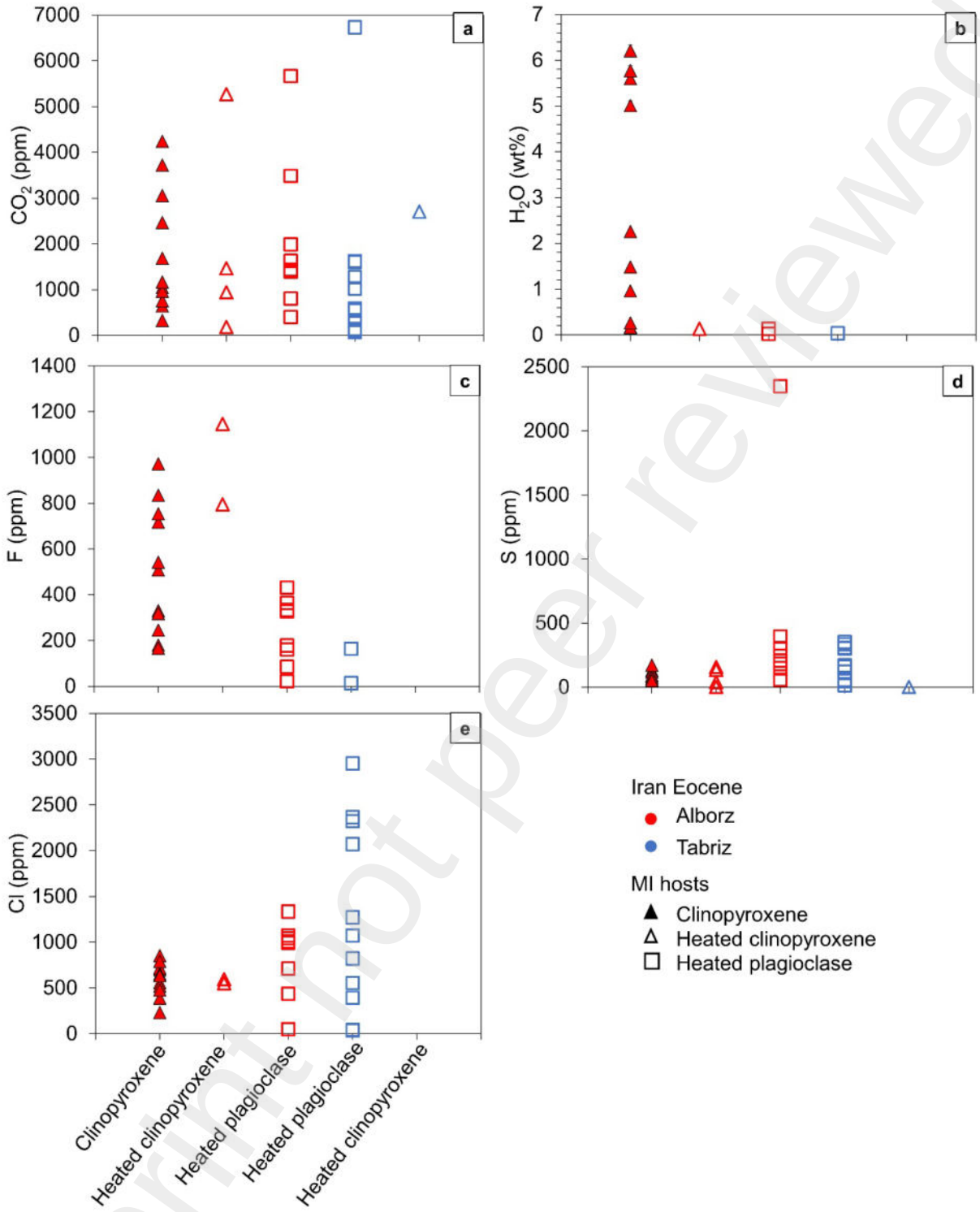

1243

1244 **Figure 5**

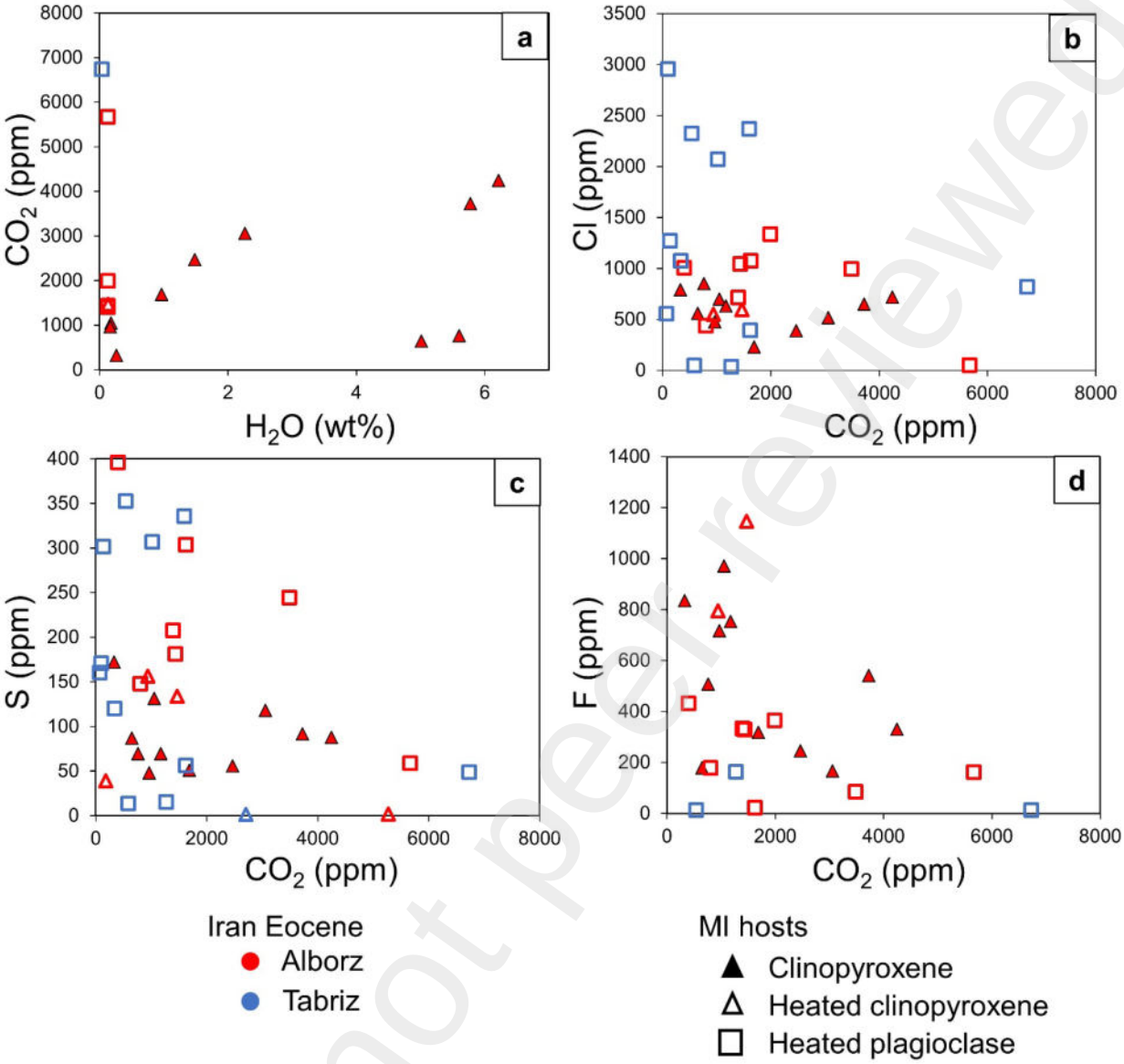

1245

1246 **Figure 6**

1247

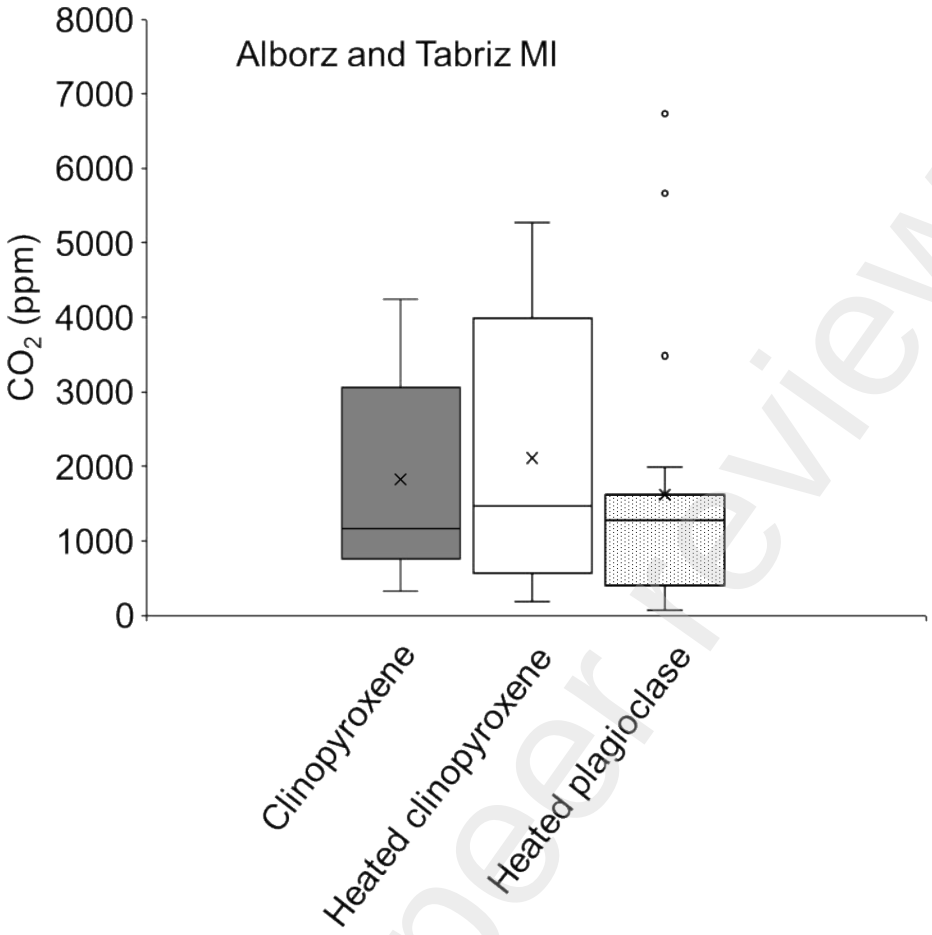

1248

1249 **Figure 7**

1250

1251

1252

1253

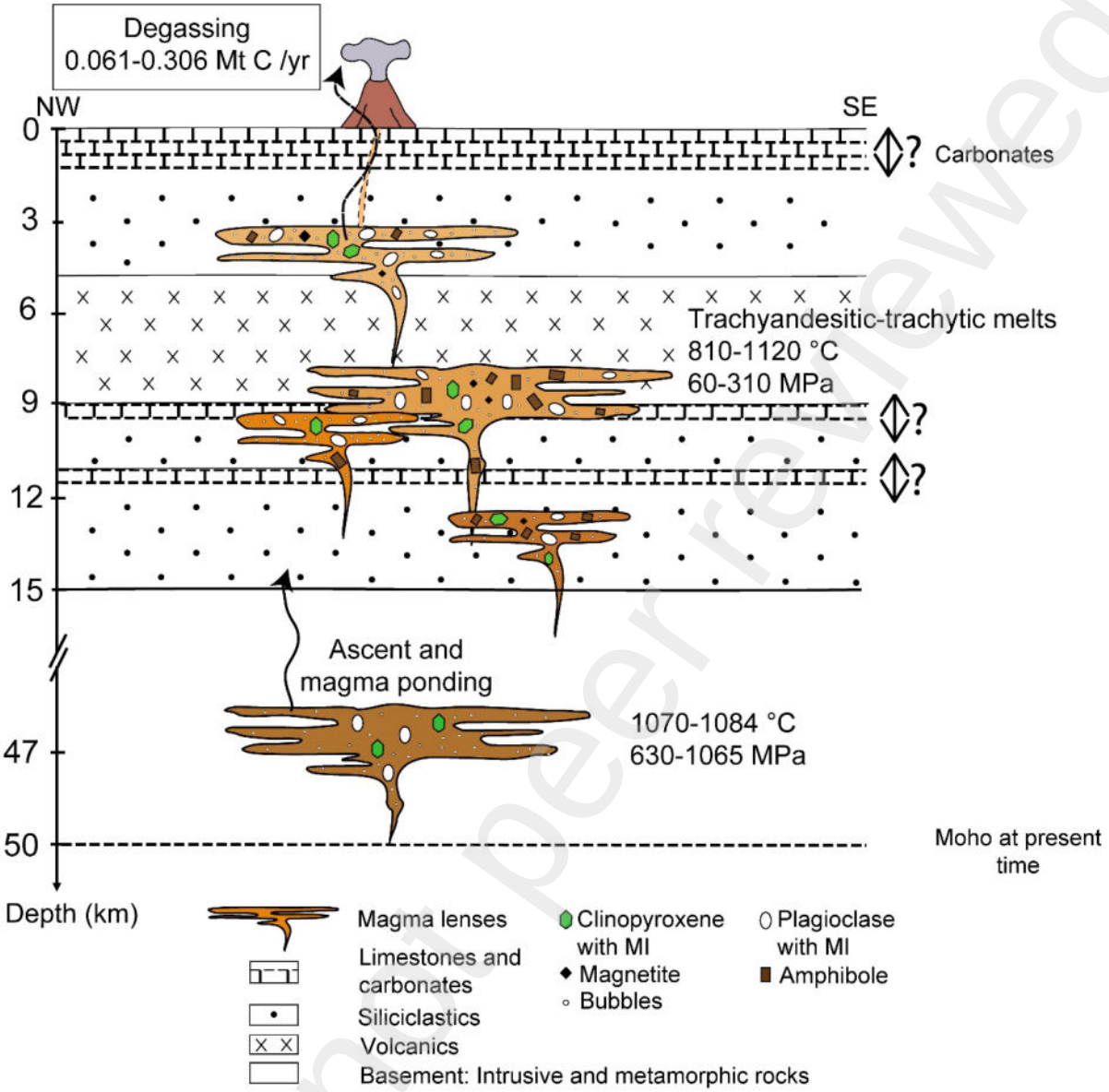

1254

1255 **Figure 8**

1256

Tables

Sample	Location	Coordinates	Nature of the sample	Approximate age
E1a, E1c	Khoja	38° 26.041'N, 46° 55.037'E	Trachyandesite	Middle-late Eocene (Geological Survey and Mineral Exploration of Iran, 2006)
PS2	Karaj Formation, Alborz Mountains	35° 57.970'N, 50° 52.932'E	Trachyandesite	Middle-late Eocene (Geological Survey and Mineral Exploration of Iran, 1995)

Table 1: Description of the samples from Iran studied here (location, coordinates (in the World Geodetic System WGS84) and nature of the samples are specified).

Temperature (°C)	Heating rate – duration during each temperature plateau	Crystal type
25-300 300-700 700-900 900-1000 1000-1100 1100-1120 1120-1130 1130-1135 1135-1140 1140-1145 1145-1150 1150-1155 1155-1160	100 °C/min – 3 min 100 °C/min – 3 min 100 °C/min – 10 min 50 °C/min – 15 min 10 °C/min – 35 min 1 °C/min – 15 min 1 °C/min – 15 min 1 °C/min – 15 min 1 °C/min – 15 min 1 °C/min – 15 min 1 °C/min – 15 min 1 °C/min – 10 min 1 °C/min – 10 min	Clinopyroxenes
25-300 300-700 700-900 900-1000 1000-1100 1100-1120 1120-1125 1125-1130 1130-1135	100 °C/min – 3 min 100 °C/min – 3 min 100 °C/min – 10 min 50 °C/min – 15 min 10 °C/min – 35 min 1 °C/min – 15 min 1 °C/min – 15 min 1 °C/min – 20 min 1 °C/min – 15 min	Feldspars

Table 2: Heating ramps used for experiments on crystals from Iran. The durations of maintaining the temperature constant after each temperature step are also specified.

Sample	PS2 (Alborz)	E1a (Tabriz)	E1c (Tabriz)
Nature	Trachyandesite	Trachyandesite	Trachyandesite
SiO_2 (wt%)	54.88	53.54	54.67
TiO_2 (wt%)	0.92	0.94	0.95
Al_2O_3 (wt%)	18.78	17.54	16.33
Fe_2O_3 (wt%)	6.15	7.44	8.71
MnO (wt%)	0.1	0.2	0.16
MgO (wt%)	1.94	1.37	2.29
CaO (wt%)	6.83	5.65	5.27
Na_2O (wt%)	3.33	4.17	3.88
K_2O (wt%)	3.82	4.57	4.11
P_2O_5 (wt%)	0.47	0.62	0.49
Cr_2O_3 (wt%)	0.023	<0.002	<0.002
Ba (ppm)	639	674	630
Ni (ppm)	<20	<20	<20
Sr (ppm)	610	502	450
Zr (ppm)	219	203	191
Y (ppm)	26	29	31
Nb (ppm)	15	11	10
Sc (ppm)	14	14	16
LOI (wt%)	2.5	3.7	2.8
Total	99.88	99.89	99.85

Table 3: Whole rock major and trace elements of the Iranian samples from Alborz and Tabriz. The sampling locations are specified in Table 1. Analyses have been performed at Bureau Veritas Mineral Laboratories (Canada) by ICP-OES (Inductively Coupled Plasma-Optical Emission Spectrometry). The type of deposit is specified. Data are expressed with total Fe as Fe^{3+} with LOI detailed.

Iran						Relative uncertainty (%)
Volume emitted over 9 My (45-36 Myr) (van der Boon. 2021) (km^3)	Minimum		Maximum			
	7.6×10^4		3.8×10^5			
Average density Iran magmas ($g.cm^{-3}$) (using the Igpet software; Carr and Gazel. 2017)	2.32					
Total erupted mass over the last eruption (t)	Minimum		Maximum			
	1.76×10^{14}		8.82×10^{14}			
Average fractionation (%) (Macdonald et al., 2008)	70					
Total mass of parental magma (t) taking the minimum and maximum volume erupted over the last eruption	Minimum		Maximum			
	3×10^{14}		1.5×10^{15}			
Measured CO_2 content from SIMS (ppm)	Minimum	Maximum	Minimum	Maximum	Average	
	76	6733	76	6733	1757	1
Calculated CO_2 flux (t/d) assuming CO_2 contents of MI from Iran	9.25×10^5	8.19×10^7	4.62×10^6	4.10×10^8	1.07×10^8 (using the maximum mass of magma)	4
Total emission (g CO_2)	2.28×10^{16}	2.02×10^{18}	1.14×10^{17}	1.01×10^{19}	2.63×10^{18}	4
CO_2 flux (Mt CO_2/yr)	0.003	0.22	0.01	1.12	0.29	4
Total emission (g C)	6.22×10^{15}	5.51×10^{17}	3.11×10^{16}	2.75×10^{18}	7.19×10^{17}	4
Carbon flux (Mt C/yr)	0.001	0.06	0.003	0.306	0.080	4

Table 4: Magmatic CO_2 flux mass balance calculations for Iran magmas assuming CO_2 concentrations of MI by SIMS. CO_2 values could be higher considering CO_2 released from carbonate sediments.

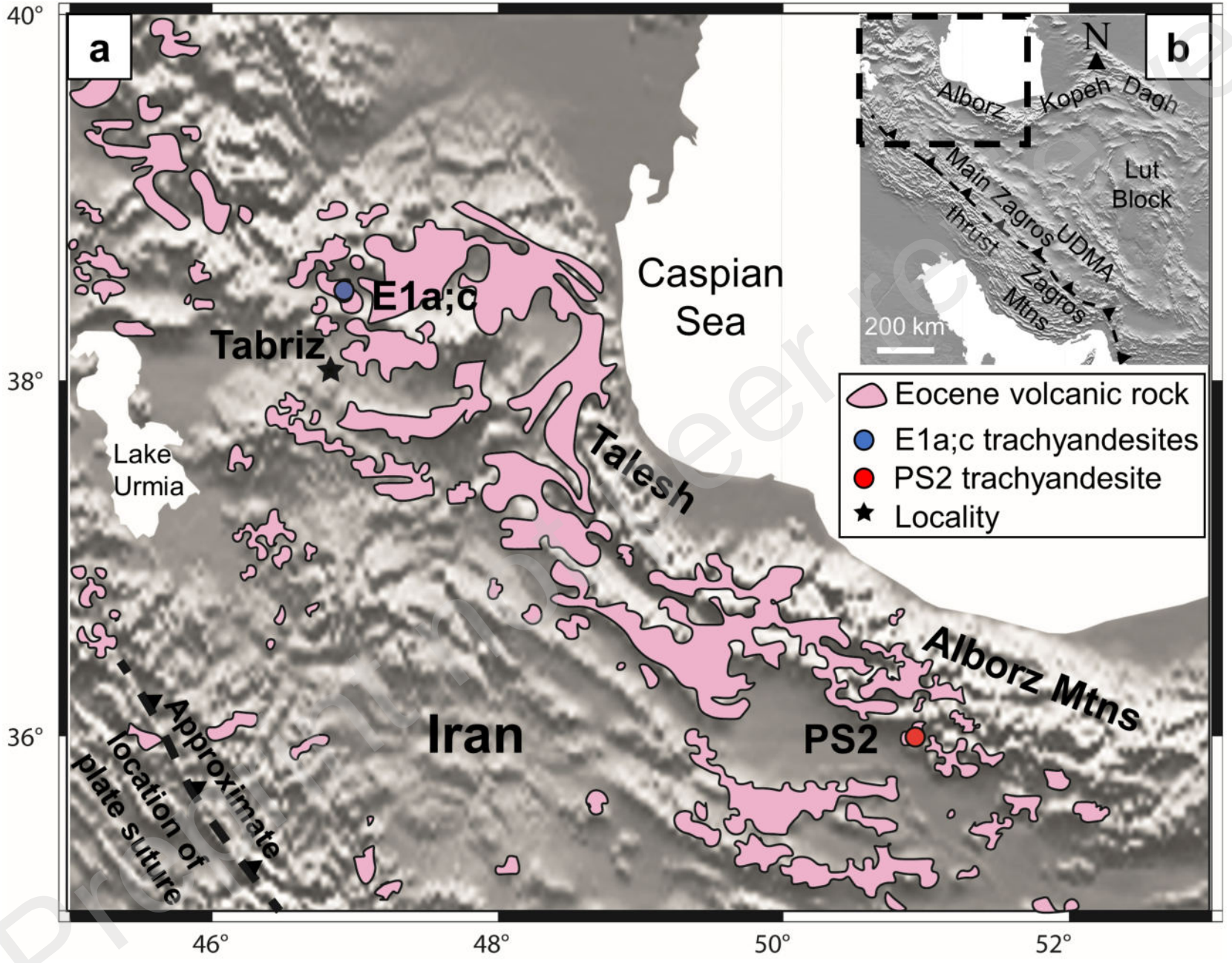

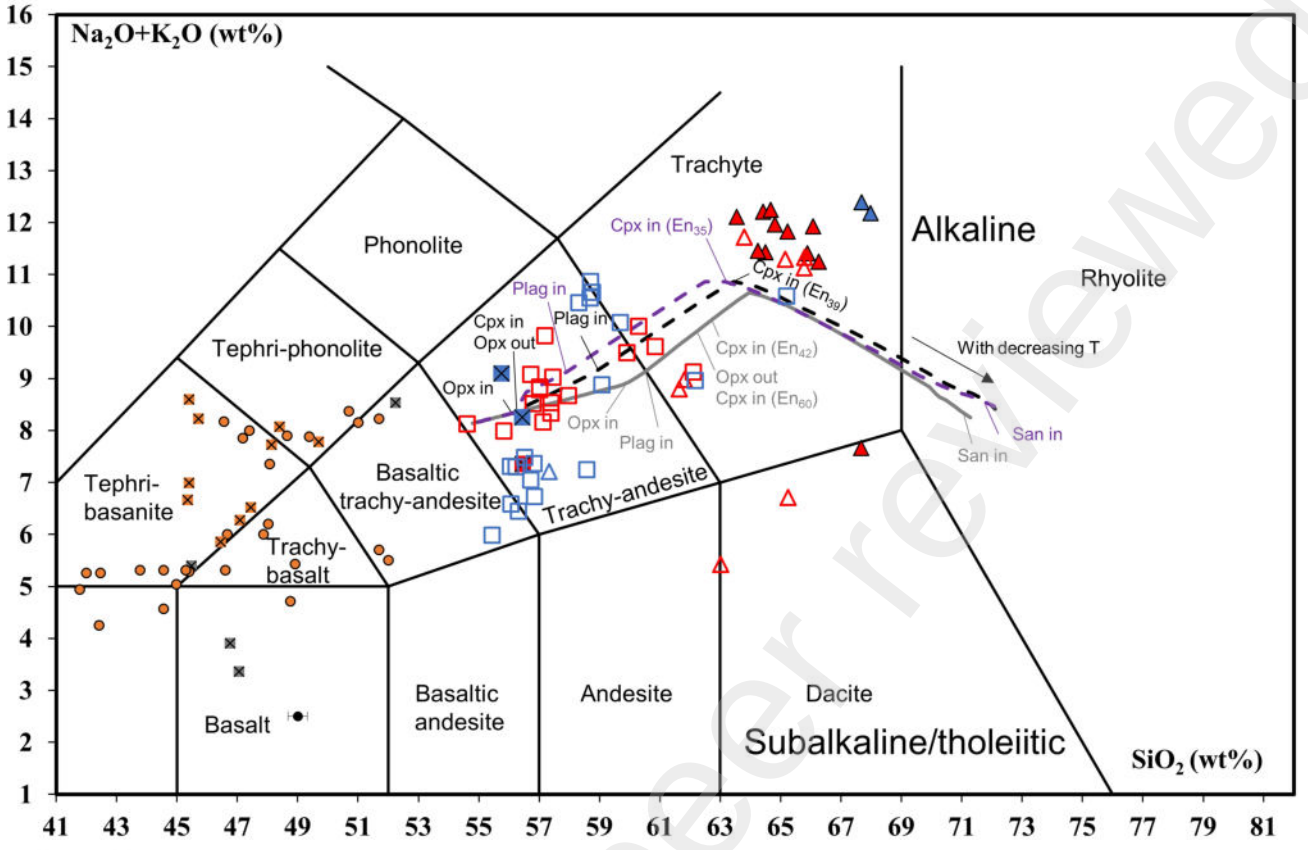

Iran Eocene
- Alborz
- Tabriz

MI hosts
- Clinopyroxene
- Heated clinopyroxene
- Heated feldspar
- Whole rock

Rhyolite-MELTS simulations
- Basaltic trachy-andesite MI – no buffer
- Basaltic trachy-andesite MI – NNO
- Basaltic trachy-andesite MI – QFM

Literature data on Iran
- Alborz Paleogene lavas (Verdel et al., 2011)
- Pliocene-Quaternary Qorveh-Bijar belt lavas (Salehi et al., 2020)
- Pliocene-Quaternary Qorveh-Bijar belt olivines-hosted MI (Salehi et al., 2020)